Appendix A

Scanning Probe Microscopes

Scanning probe methods have developed into ubiquitous tools in surface science and, the range of phenomena investigated by these techniques is continuing to grow. These include surface topography, electronic and vibrational properties, films growth, and measurements of adhesion and strength of individual chemical bonds, friction, studies of lubrication, dielectric and magnetic properties, contact charging, molecular manipulations and, many other phenomena from the micrometer down to the sub-nanometer scale. For the characterizations of the nanostructures *Scanning Probe Microscope* (SPM) [1] has been applied. SPM is well-known example of a technique which can contribute to the most important aspects of nanotechnology: imaging, modifying and manipulating matter on the nanometer-scale [2]. The family of SPM techniques is very diverse, with different methods specializing in different surface properties. Until now, the various SPMs are invented such as *Magnetic Force Microscope* (MFM) for magnetic field [3], *Scanning Capacitance Microscope* (SCM) for capacitance [4], *Scanning Near-field Optical Microscope* (SNOM) for optical properties [5], *Atomic Force Microscope* (AFM) for surface topography and the fabrication of structures [6], *Friction Force Microscope* (FFM) for the characteristics of the friction forces between

two bodies (tip and sample) [7] and etc.

AFM and *Nanoindenter*, members of SPM group, are significantly tools to scientific researches and applications for the topography diagnostics, the mechanical properties and fabrication mechanisms of materials. In this section, the historical background and operational principles of AFM and Nanoindenter are introduced.

A-1 Atomic Force Microscope

Soon after *Scanning Tunneling Microscope* (STM) was invented, it was evident that a similar kind of scanning microscope was needed that could be used for non-conductor surfaces. Historically, there were some inventions that operated on principles which could be useful as a basis for such instrumentation. The general principle of operation is almost similar in STM and AFM. The first AFM was developed five years after the introduction of the STM [8-9]. Based on the same principles as for STM, the AFM was later developed for non-conducting solid surfaces [8].

Therefore, AFM can operate on conducting and non-conducting surfaces [7]. Most often, a micro-machined cantilever with a sharp tip on the edge is used as the probe, and either the sample or the probe is mounted on a piezoelectric tube that acts as a 3D actuator. Cantilever deflection due to tip-sample interaction is measured by casting a laser beam on the cantilever and detecting the reflected beam with a position sensitive detector (PSD) [10], please see Fig.A1(a).

A variety of tip-sample surface interactions may be measured by an AFM, depending on the separation between tip and sample. At short distances the tip mainly experiences interatomic forces: the very short range (~0.1nm) Born repulsive forces and the longer range (up to 10nm) van-der-Waal (vdW) forces. At distances of a few

nanometers, vdW forces are sufficiently strong to move macroscopic objects, such as AFM cantilevers. vdW interactions consist of three components: polarization, induction and dispersion forces. For two identical interacting gas molecules, for example, the vdW potential can be expressed as the sum of three components as:

$$U_{vdW} = -\left(\frac{1}{4\pi\varepsilon_0}\right)^2\left(\frac{\mu^4}{3kT} + 2\mu^2\alpha + \frac{3}{4}\alpha^2\hbar w\right)\frac{1}{z^6} \approx -\frac{C_1}{z^6} \tag{A1}$$

where ε_0, T, μ and α are denoted as the permittivity of vacuum, the temperature, the permanent dipolar moment and the polarizability of the molecules, respectively. $\hbar w$ is the ground state energy of electrons, z is the distance between the interacting molecules and C_1 is the London coefficient.

Describing the AFM tip and sample interactions, the attractive and repulsive potential pairs have to be summed for all interacting atoms with consideration of the local geometry, material properties and experimental force *vs*. distance curve is applied, that can be registered by AFM while approaching the tip towards the sample. Typical variation of the tip-sample interaction force with the separation in between them is illustrated in Fig.A1(b). The vdW potential between two macroscopic bodies, for example a sphere (like the AFM tip end) and a plane (the sample surface), can be approximated as [11]:

$$U_{vdW} = -\left(\frac{AR}{6z}\right) \tag{A2}$$

and the vdW force as:

$$F_{vdW} = -\frac{dU_{vdW}}{dz} = -\frac{AR}{6z^2} \tag{A3}$$

where R is the radius of the sphere and A is the Hamaker constant, $A \approx \pi^2 C_1 \rho_1 \rho_2$, that characterizes the properties of the interacting materials. ρ_1 and ρ_2 are the densities of the interacting bodies.

Two distance regimes are labeled on Fig.A1(b): 1.) the contact regime and 2.) the

non-contact regime. In the contact regime, the cantilever is held less than a few Å from the sample surface and the interatomic force between the cantilever and the sample is repulsive. In the non-contact regime, the cantilever is held on the order of tens to hundreds of Ås from the sample surface, and the interatomic force between the cantilever and sample is attractive.

AFM operates in the following way: the AFM tip is in direct contact with the sample and measures the force between sample and tip. Compared to the STM, this alternative approach to the feedback is a major advantage for the AFM and enables the investigation of all kinds of materials ranging from insulators to living cells. Typically, pyramidal silicon nitride tips are used, which have a radius of curvature on the order of 100Å. The Si_3N_4 cantilever of an approximate 200μm length and a spring constant of 0.06N/m or 0.12N/m are generally used. Recently, much research has been carried out on improving the shape and other characteristics of the cantilever. AFM has thus become a versatile modern technique of immense applications in such areas as surface science.

∫ Contact mode

In contact AFM (cAFM) mode, also known as repulsive mode, an AFM tip makes soft "physical contact" with the sample. The tip is attracted to the end of a cantilever with a low spring constant, lower than the effective spring constant holding the atoms of the sample together. As the scanner gently the tip across the sample, the contact force causes the cantilever to bend to accommodate changes in topography. To examine this in more detail, refer to the Fig.A1(b).

At the right side of the curve the atoms are separated by a large distance. As the atoms are gradually brought together, they first weakly attract each other. This attraction increases until the atoms are so close together that their electron clouds

begin to repel each other electrostatically. This electrostatic repulsion progressively weakens the attractive force as the interatomic separation continues to decrease. The force goes to zero as the distance between the atoms reaches a couple of angstroms, about the length of a chemical bond. When the total vdW force becomes positive (repulsive), the atoms are in contact. The slope of the vdW curve is very sharp in the contact regime. Consequently, the repulsive vdW force balances almost any force that attempts to push the atoms closer together. In AFM this means that when the cantilever pushes the tip against the sample, the cantilever bends rather than forcing the tip atoms closer to the sample atoms. Even if you design a very stiff cantilever to exert large forces on the sample, the interatomic separation between the tip and the sample atoms is unlikely to decrease much.

The AFM tip itself consists of a cantilever that supports the tip. The cantilever is connected to a bulk region needed for the handling of the AFM tips with tweezers. Normally the whole system consisting of tip, cantilever and bulk, is fabricated of the same material, commonly silicon. In a simple picture, the cantilever is described as a leaf spring with a characteristic spring constant k. In the contact mode, a contact force F_C is applied between the tip and the sample surface during the scanning of the surface with xyz-piezo-resistive crystal. A simple idealizes picture of this process is shown in Fig.A1(a). With the spring constant k of the cantilever the force F_C is easily calculated with Hooke's law: $F_C=k\triangle z$, where $\triangle z$ is the deflection of the cantilever out of equilibrium. The AFM feedback loop measures the contact force between the tip and the surface with the help of a laser that is focused onto the cantilever. The laser beam is reflected at the cantilever top and shines onto a photo detector. The deflection and thus the change of the contact force is monitored by measuring the voltage variation dV at the detector, Fig.A1(a). The height information is obtained by recording the voltages applied to the z-piezo, which are needed to keep the signal of

the photo detector constant. Finally, the sample topography is visualized by converting the voltage applied to the *z*-piezo into height information *dz* and plotting the data array in a color-coded image.

The cAFM mode successfully performed many pioneering AFM applications; however, it suffers from several drawbacks. The constant downward force of the tip onto the sample surface is not always low enough to avoid damaging certain sample surfaces.

∫ Non-contact mode

The non-contact mode AFM (ncAFM)**,** invented in 1987 [12], offers unique advantages over other contemporary scanning probe techniques such as cAFM and STM. ncAFM is one of several vibrating cantilever techniques in which an AFM cantilever is vibrated near the sample surface. The spacing between the tip and the sample for non-contact mode is on the order of tens to hundreds of Ås. This spacing is indicated on the vdW curve of Fig.A1(b) as the non-contact regime.

The ncAFM is desirable because it provides a means for measuring sample topography with little or no contact between the tip and the sample. Like cAFM, ncAFM can be used to measure the topography of insulators and semiconductors as well as conductors. The total force between the tip and the sample in the non-contact regime is very low, which is advantageous for studying soft or elastic samples. In ncAFM mode, the system monitors the resonant frequency (typically from 100 to 400kHz) or vibrational amplitude of the cantilever and keeps it constant with the aid of a feedback system that moves the scanner up and down. By keeping the resonant frequency or amplitude constant, the system also keeps the average tip-to-sample distance constant. As with cAFM, the motion of the scanner is used to generate the data set.

§ Tapping mode

Tapping mode AFM (tAFM) is similar to ncAFM, except that for tAFM the vibrating cantilever tip is brought closer to the sample so that at the bottom of its travel it just barely hits, or "taps" the sample. The tAFM operating region is indicated on the vdW curve in Fig.A1(b). As for ncAFM, for tAFM the cantilever's oscillation amplitude changes in response to tip-to-sample spacing. An image representing surface topography is obtained by monitoring these changes. Some samples are best handled using tAFM instead of contact or ncAFM. tAFM is less likely to damage the sample than cAFM because it eliminates lateral forces between the tip and the sample. In general, it has been found that tAFM is more effective than ncAFM for imaging larger scan sizes that may include greater variation in sample topography. tAFM has become an important AFM technique since it overcomes some of the limitations of both cAFM and ncAFM.

In closing, the contact mode is generally used in most AFM procedures. Contact mode can also be operated under fluids with similar high resolution to that in air. The tapping mode is achieved by oscillating the tip close to its resonance frequency. This has provided much improvement in images in some systems. In non-contact mode, the tip is never in contact with the substrate, which differs from the contact mode. This mode is found to be most suitable for soft materials. The probe encounters the attractive and the repulsive force field of the sample during a period of vibration of the cantilever is called the tapping mode. The interactions forces, attractive or repulsive, as small as few nano-Newtons between the cantilever and the sample can be measured. In the non-contact mode, the net force detected is the attractive force between the tip and the sample. On the other hand, in the contact mode, the net force measured is the sum of the attractive and repulsive forces. Thus, these two modes are different as follows:

- Contact mode: attractive forces + repulsive forces
- Non-contact mode: attractive forces

As above mentioned, due to these capabilities the AFM became one of the most important tools for the analysis of surfaces in research and industrial applications.

In this dissertation, a SPM (CP-R SPM, USA) apparatus is used to measure the topographic properties of the samples. AFM scanning uses only the two vertical quadrants to measure vertical deflection of the cantilever thus showing the surface profile of the sample. For each AFM operation, a constant scan speed of 1μm/s was used with a constant load of 30nN applied to the cantilever. The measurement tip is made of Si_3N_4 with a cantilever of lower stiffness and thus yielding measurements of greater sensitivity. AFM instrument and an AFM tip are illustrated in Figs.A2(a)-(b).

A-2 Nanoindenter

Depth-sensing Indentation (DSI), instrumented indentation, continuously recording indentation technique, mechanical properties microscope, ultralow-load indentation: all these names are used interchangeably in literature for the same testing technique. If indentations are performed in the nanometer-scale depth range it is usually referred to as *nanoindentation.* A diamond tip is pressed into the sample surface and, subsequently, after having reached a given maximum depth or maximum load, the tip is moved. During the procedure, the load on, as well as the displacement of, the indenter are recorded. Results of such an experiment is therefore not only the value of hardness but the complete history of the deformations occurring during this indentation test, as saved in the so-called load-displacement curve of Fig.A3. This load-displacement curve consists of a loading and an unloading curve. The loading curve characterizes

the resistance of the sample against the penetration of the tip into the material and reflects both the elastic and the plastic properties of the tested material. The unloading curve is mainly determined by elastic recovery of the indent. From such the curve hardness and the Young's modulus of the material can be determined by using an appropriate analysis model. Thus, two prerequisites are necessary for a successful application of the DSI technique: an apparatus capable of performing indentation experiments while simultaneously recording the applied load and the corresponding displacement of the indenter and a method for the analysis of the measured load-displacement curves.

§§ How nanoindentation works?!

(a) The SPM tip is moved along the sample to create an image of the surface, please see Fig.A4(a).

(b) While imaging, the tip is free to move up and down since no load is being applied, please see Fig.A4(b).

(c) An indentation is made by charging the distance between capacitance (which the Hysitron system reads as a load) which forces the diamond tip down into the sample; please see Fig.A4(c).

§ Hysitron NanoIndenter

The Hysitron TriboScope is an add-on-DSI system to a commercial SPM (Triboscope, Hysitron Inc., USA); consisting of a force-displacement transducer, a transducer controller and a computer, please see Fig.A3. In addition, the specifications and features of the Hysitron TriboIndenter are given in Table A1. The SPM software is used to interpret the voltage signal from the transducer, and the microscope piezos enable displacement control as imaging. The combination of the DSI system with a

SPM has a symbiotic effect: it extends the SPM in the capability of making DSI experiments with a high load (100nN) and depth resolution (0.2nm) and, it enables the DSI system to take images of the sample surface by using the same diamond tip for imaging and for indentation.

The heart of the Hysitron TriboScope NanoIndenter is a three plate capacitive force-displacement transducer which is displayed in Fig.A4. It consists of two fixed drive plates and a pick-up electrode that is spring mounted to the housing. The diamond tip is mounted to the pick-up electrode which can move up and down. To perform an indentation, an electrostatic force is generated between the pick-up electrode and a drive plate. The amount of this force, F_{el}, is proportional to the square of the voltage applied to the drive plate, V [13]:

$$F_{el} = k_e \cdot V^2 \tag{A4}$$

where the k_e is an electrostatic force constant. It is determined by the manufacturer and is supplied with the transducer. Using k_e, the force-time scheme set by the operator is translated by the control software into a voltage-time scheme which is than applied to the transducer. During the indentation process, the load on and, the displacement of, the indenter are measured as a function of time. From the load-time and the displacement-time plots, the corresponding load-displacement curve is obtained. The nanoindenter instruments are illustrated in Figs.A5(a)-(c).

§ MTS NanoIndenter

Nanoindenter is operated by MTS TestWork® instrument control environment, please see Fig.A6, which is common to all MTS test equipment and allows the user infinite flexibility in the specification of test procedure and data analysis. The sample is mounted on an accuracy controlled *x-y* stage for precise positioning of indents. Force

and displacement versus time are recorded during the cycle of indentation from which standard output, e.g. hardness and elastic modulus (Oliver-Pharr method), calculation of hardness and modulus as a function of penetration depth.

Accessories

- CSM (Continuous Stiffness Measurement) performs modulus calculation at hundreds of points during a single indent.
- DCM (Dynamic Control Modulus) allows highest resolution testing.
- High Load allows loading up to 500mN without loss of resolution.

Specifications

- CSM: Maximum depth—500μm; Depth resolution—< 0.01nm;
  Maximum load—500mN; Load resolution—50nN.
- DCM: Maximum depth—15μm; Depth resolution—0.0002nm;
  Maximum load—10mN; Load resolution—1nN.

Hysitron Nanoindenter monitors and records the load and displacement of the indenter, a diamond Berkovich three-sided pyramid, with a force resolution of about 50nN and displacement resolution of about 0.1nm. A triangular pyramid (Berkovich) diamond indenter was employed for all experiments, which is preferred over the four-sided Vickers or Knoop indenter because a three-sided pyramid is more easily ground to a sharp point [14]. This post-test *in-situ* imaging capability provides the ability to verify that the tests were performed in the anticipated location, which maximizes the reliability of record and aids in explanation of unexpected test results. Hardness and elastic modulus were calculated from the recorded load-displacement curves. The indentation impressions were then imaged *in-situ* using the same indenter tip. A typical indentation experiment consists of four subsequent steps: approaching the surface; loading to peak load at a loading rate of 10μN/s; holding the indenter at

peak load for 10s; finally unloading completely. The hold step was included to avoid the influence of creep on the unloading characteristics since the unloading curve was used to obtain the elastic modulus of a material. For more details on nanoindentation experimental techniques, please see Ref.15. All nanoindentation tests were performed when the thermal drift dropped down to 0.01nm/s. The thermal drift effects were corrected for each test using a holding segment in the air before indentation.

On the other hand, though many mechanisms have been proposed, a large amount of influencing factors in microstructures and experiments make it impossible to find a dominant mechanism suitable for every system investigated. For instance, the nanohardness could be overestimated since the substrate effects may be overwhelming for larger penetration depth, and discontinuous measurement makes it difficult to define the initial slope of unloading curve. Thus, CSM technique [16-17] is required in nanoindentation measurements. This technique is accomplished by imposing a small, sinusoidally varying single in top of DC single, for driving the motion of the indenter. The records are obtained by analyzing the response of the system using a frequency-specific amplifier. This technique allows the measurement of contact stiffness at any point along the loading curve and not just at the point of unloading as in the conventional measurement. In CSM technique of MTS NanoIndenter® XP, a harmonic force is superimposed to the normal applied force. This oscillated force with known phase and amplitude interacts with the sample, which responds with a displacement phase and amplitude characteristic of the stiffness and damping of contact with the indenter. Thus, the stiffness data along with load and displacement curve are recorded. The hardness and elastic modulus can be calculated using the CSM stiffness data acquired during the indentation experiment. Hence, CSM allows hardness and elastic modulus to be determined as a function of penetration depth with a single indentation load/unload cycle.

For MTS NanoIndenter® XP, the cyclic tests were performed in following manner: loading to the maximum load and unloading by 90%; reloading to the maximum load and unloading by 95%; hold for 30sec at 10% of the maximum load for thermal drift correction and complete unloading. The maximum indentation loads used were 80-200mN for all materials, please see Fig.A7(a).

Currently, two variants of the method are in use: (i) with monotonic loading and unloading, in which the elastic modulus and hardness are determined from the unloading curve, and (ii) CSM mode that a small harmonic signal is added to the monotonically increasing basic load. The latter method makes possible the continuous determination of properties during loading from "zero" to the maximum indentation load. This can be especially useful for samples whose properties change with depth since the variation of properties with depth can be obtained through a single test. The difference of operation model of Hysitron (Fig.A7(b)) and MTS-CSM technique (Fig.A7(c)) NanoIndenters can be clearly displayed, which the load-displacement curve of GaN are presented.

§ Tips

The tip is a very important part of nanoindentation testing. Indenters with various tip shapes are used in indentation testing: sphere, 4-sided pyramids and cones. In nanoindentation testing 3-sided pyramids are usually used, because they are easier to fabricate with sharp tips than 4-sided pyramids. Several types and parameters of the indentation tips are presented in Fig.A8 and Table A2 [18].

Probe tips are even more important in nanoindentation, for the material properties are calculated based upon their dimensions. Tips of the same geometry as macroscopic testing are used at this scale: spheres, flat punches, cones and pyramids. Spherical tips are not self-similar; therefore the induced strain increases with

indentation penetration depth. This leads to scaling of the hardness with indentation penetration depth in materials that strain harden. Pyramidal and conical indenters are self-similar and, the ration of radius to depth is constant. Theoretically materials that have homogeneous hardness should have the same result independent of indentation penetration depth. It is common for hardness to change with indentation load or depth, even in the case of self similar tips. There is one significant difference in the pyramidal indenters used in nanoindentation. Three sided objects always meet at a point. The radius of the apex is critical because it dictates the contact area. Tips are usually categorized as shape and blunt. A sharp tip hat may reach critical stresses at very low loads, acting as a knife cutting through the material creating new surface with little elastic deformation. Also, with blunt tips elasticity plays a more important role. The larger contact area means that higher loads must be used to initiate plasticity. Depending on the properties being studied there may be an optimal tip radius.

The majority of our dissertation has been done with a Berkovich indenter tip. Fig.A9 is a sketch of the 3-sided pyramidal indenter. The Berkovich indenter tip has a face angle of 65.3^{o}, which results in an equivalent cone angle of 70.32^{o}. The face angle was chosen to give the same projected area to depth ratio of a Vickers indenter. A typical Berkovich indenter has a radius on the order of 50nm [19], which is supplied from *Advanced Semiconductor Engineering (ASE) Group-Stress LAB.*

Reference

1. D. Bonnell, *Scanning Probe Microscopy and Spectroscopy: Theory, Techniques and Applications* (John Wiley & Sons Inc., New York, 2001).
2. C.F. Quate, Jpn. J. Appl. Phys. 42 (2003) 4777.
3. F. Pedreschi, J.M. Sturm, J.D. O'Mahony and C.F. J. Flipse, J. Appl. Phys. 94 (2003) 3446.
4. P.A. Rosenthal, Y. Taur and E.T. Yu, Appl. Phys. Lett. 81 (2002) 3993.
5. J.M. Kim, T. Ohtani and H. Muramatsu, Surf. Sci. 549 (2004) 273.
6. M. Tachiki, T. Fukuda, K. Sugata, H. Seo, H. Umezawa and H. Kawarada, Jpn. J. Appl. Phys. 39 (2000) 4631.
7. K.S. Birdi, Ed., *Handbook of Surface & Colloid Chemistry* (CRC Press, Boca Raton, FL, 1997; 2nd ed., 2002).
8. G. Binnig, H. Rohrer, Ch. Gerber and E. Weibel, Phys. Rev. Lett. 50 (1983) 120.
9. K.S. Birdi, *Self-Assembly Monolayer* (*SAM*) *Structures* (Plenum Press, New York, 1999).
10. G. Meyer and N. Amer, App. Phys. Lett. 53 (1988) 2400.
11. J. Israelachvili, *Intermolecular & Surface Forces* (Academic Press Inc., San Diego, CA 92101, 1991).
12. Y. Martin, C.C. Williams and H.K. Wickramasinghe, J. Appl. Phys. 61 (1987) 4723.
13. B. Bhushan, A.V. Kulkarni, W. Bonin and J.T. Wyrobek, Phil. Mag. A 74 (1996) 1117.
14. G.M. Pharr, Mater. Sci. Eng. A 253 (1998) 151.
15. X. Li and B. Bhushan, Mater. Charact. 48 (2002) 36.
16. X. Li and B. Bhushan, Mater. Charact. 48 (2002) 11.
17. R. Saha and W.D. Nix, Acta Mater. 50 (2002) 23.
18. A.C. Fischer-Cripps, *Nanoindentation* (New York, Springer, 2004).
19. N.R. Moody, W.W. Gerberich, N. Burnham and S.P. Baker, *Fundamentals of Nanoindentation and Nanotribology* (Materials Research Society, Warrendale, PA, 1998).

Table and Figure Captions

Table A1. Specifications and features of the Hysitron TriboIndenter.

Force	
Maximum	30 mN, 500 mN
Minimum Contact Force	1 nN
Resolution	$<$1 nN
Noise Floor	$<$100 nN
Displacement	
Maximum	50 μN
Resolution	0.0002 nm
Noise Floor	0.2 nm
Positioning	
Placement of Indents	$\pm$ 10 nm
Field of Testing	120 mm x 100 mm
Instrument Features	
Resolution Frequency	150 Hz
Load Frame Stiffness	500000 N/m
User Interface	Windows 95/98/NT/2000
Testing Capabilities	
Constant Strain Rate Loading	yes
In-situ Topographical Imaging	yes
Dynamic Properties	yes
Temperature Control	-5 ℃ to 150 ℃

Table A2. Projected area, intercept corrections, and geometry correction factors for various types of indents. The semi-angles givens for pyramidal indenters are the face angles with the central axis of the indenter.

indentater type	projected area	semi-angle θ (deg)	effect cone angle α (deg)	intercept factor	geometry correction factor, β
Sphere	$A = 2\pi R h_c$	N/A	N/A	0.75	1
Berkovich	$A = 3\sqrt{3}\, h_c^2 \tan^2\theta$	65.3°	70.2996°	0.75	1.034
Vickers	$A = 4h_c^2 \tan^2\theta$	68°	70.32°	0.75	1.012
Cube Corner	$A = 3\sqrt{3}\, h_c^2 \tan^2\theta$	35.26°	48.28°	0.75	1.034
Cone	$A = \pi h_c^2 \tan^2\alpha$	α	α	0.72	1
Knoop	$A = 2h_c^2 \tan\theta_1 \tan\theta_2$	θ_1 =86.25° θ_2 =65°	70.64°	0.75	1.012

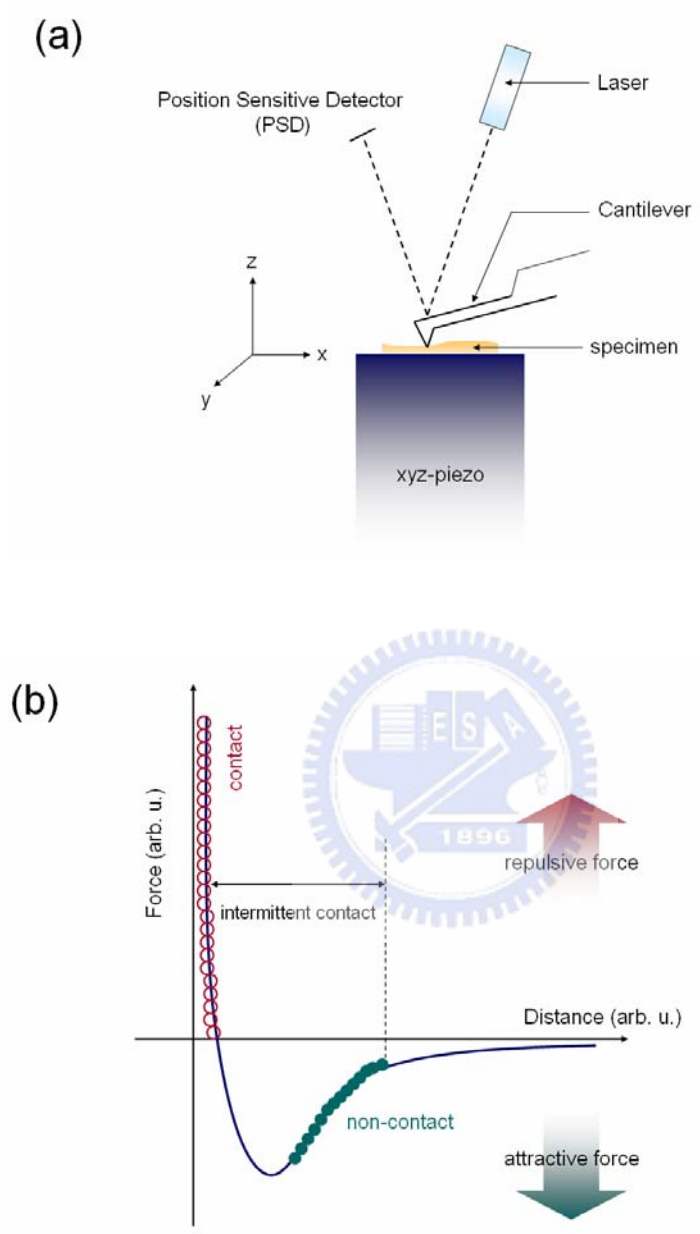

Figure A1. (a) AFM apparatus principle. Cantilever movement on a substrate under controlled constant force or other parameters; (b) Empirical force vs. distance (i.e. tip-sample separation) curve that reflects the main interactions between the scanning tip and specimen surface during AFM measurements.

(a)

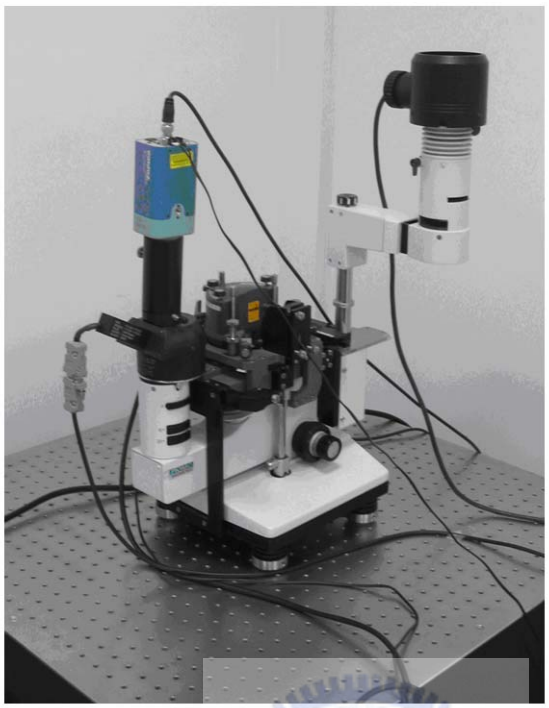

(b)

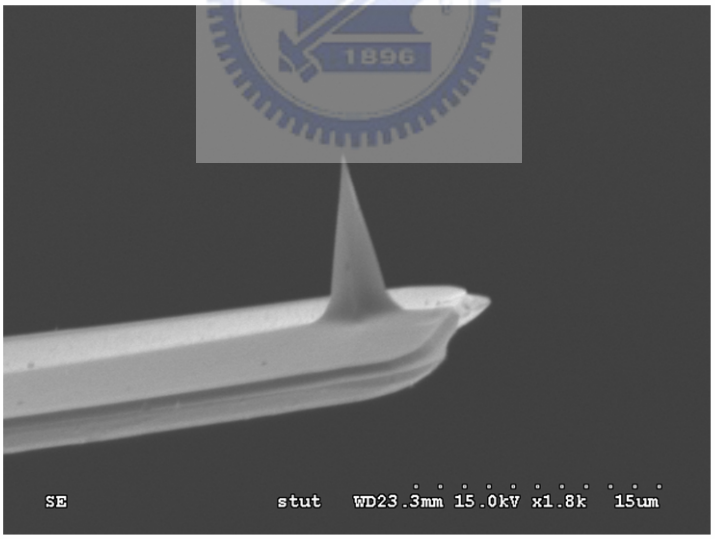

Figure A2. (a) AFM instrument and (b) an AFM tip.

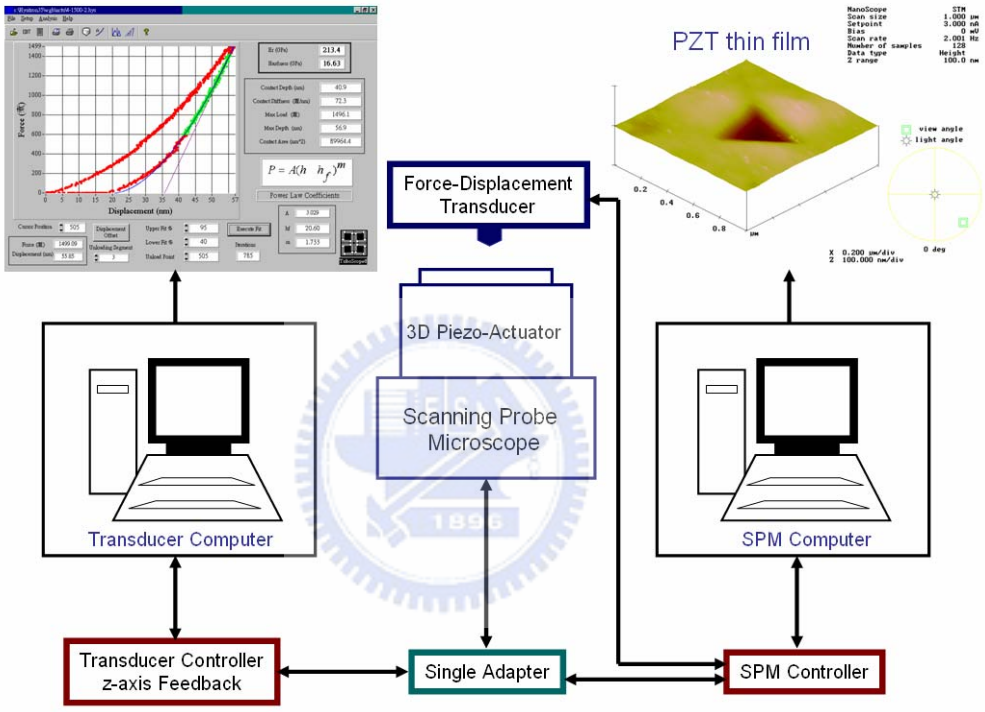

Figure A3. Schematic of the TriboScope in use with a SPM. The SPM contributes the imaging software and displacement control. The indentation system consists of the transducer, controller and a separate data acquisition system.

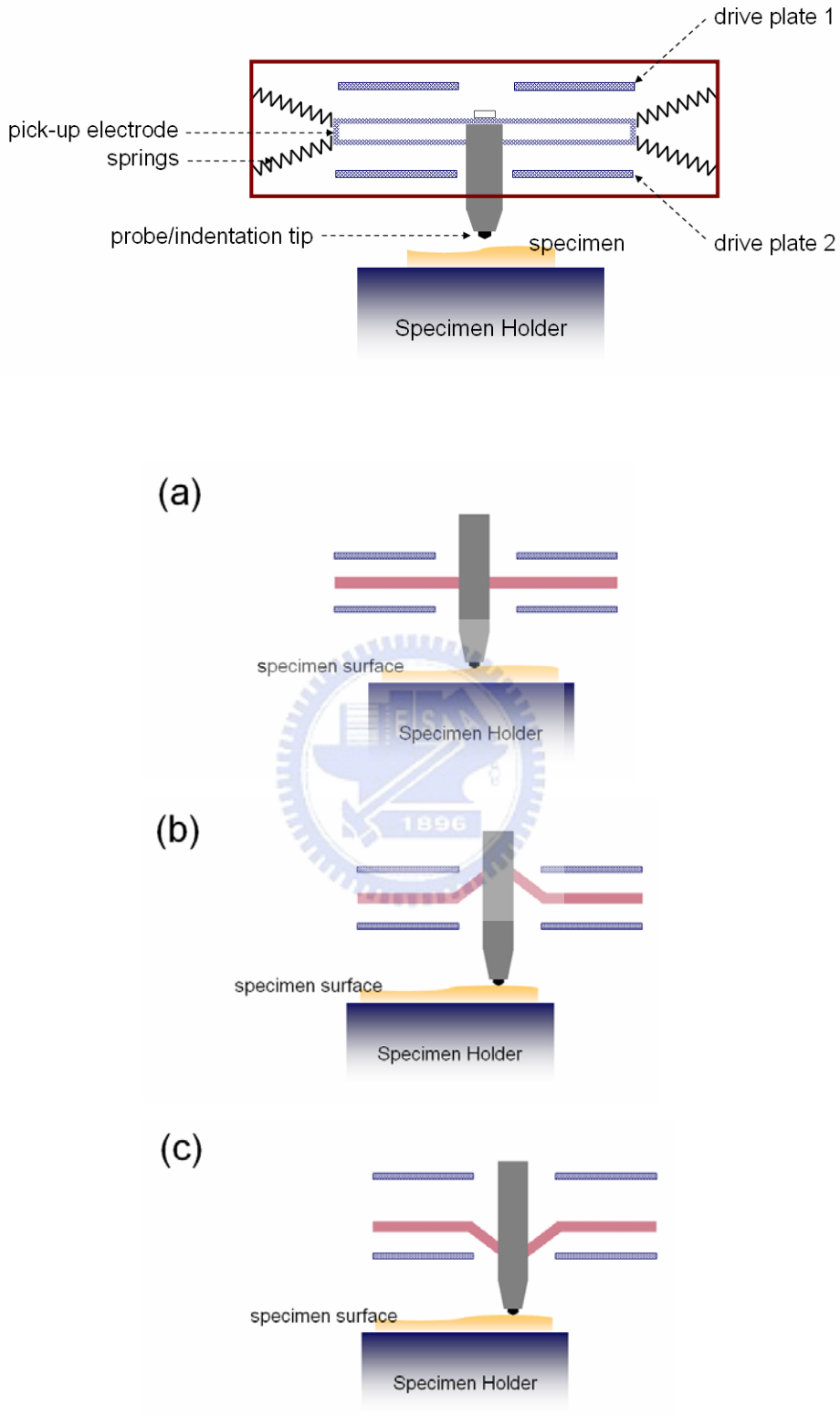

Figure A4. Schematic of the three plate capacitive force-displacement transducer of the Hysitron TriboScope. And (a)-(c): The nanoindentation works processes.

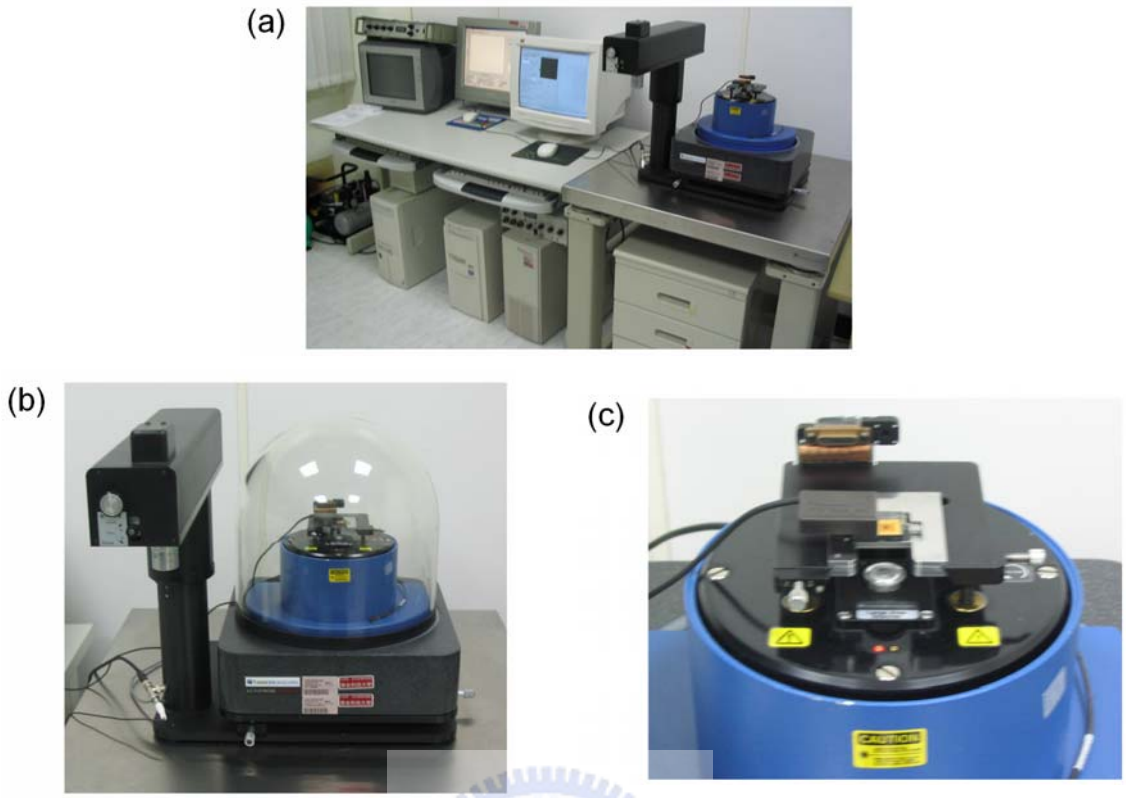

Figure A5. The Hysitron TriboScope Nanoindenter apparatus.

Figure A6. The MTS NanoIndenter® XP Nanoindenter apparatus.

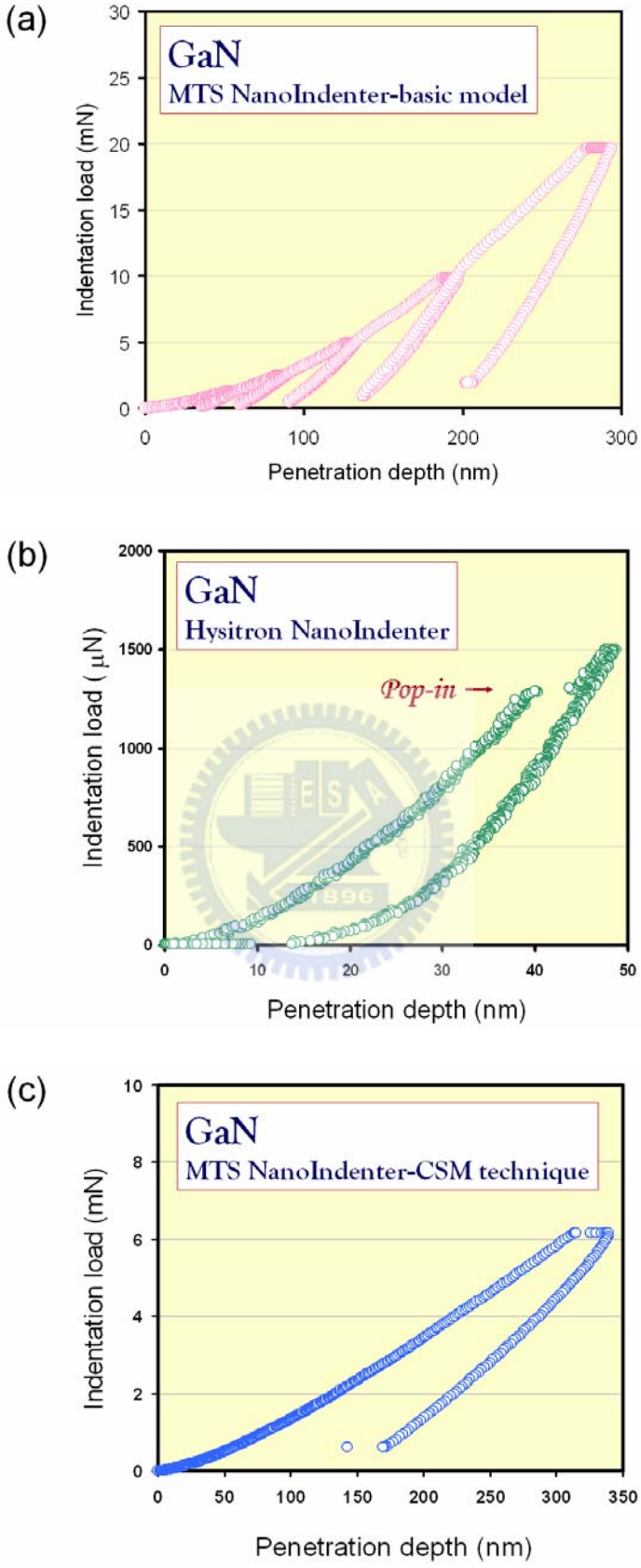

Figure A7. GaN nanoindentation with (c) MTS NanoIndenters-basic model, (b) Hysitron and (c) MTS NanoIndenters-CSM model.

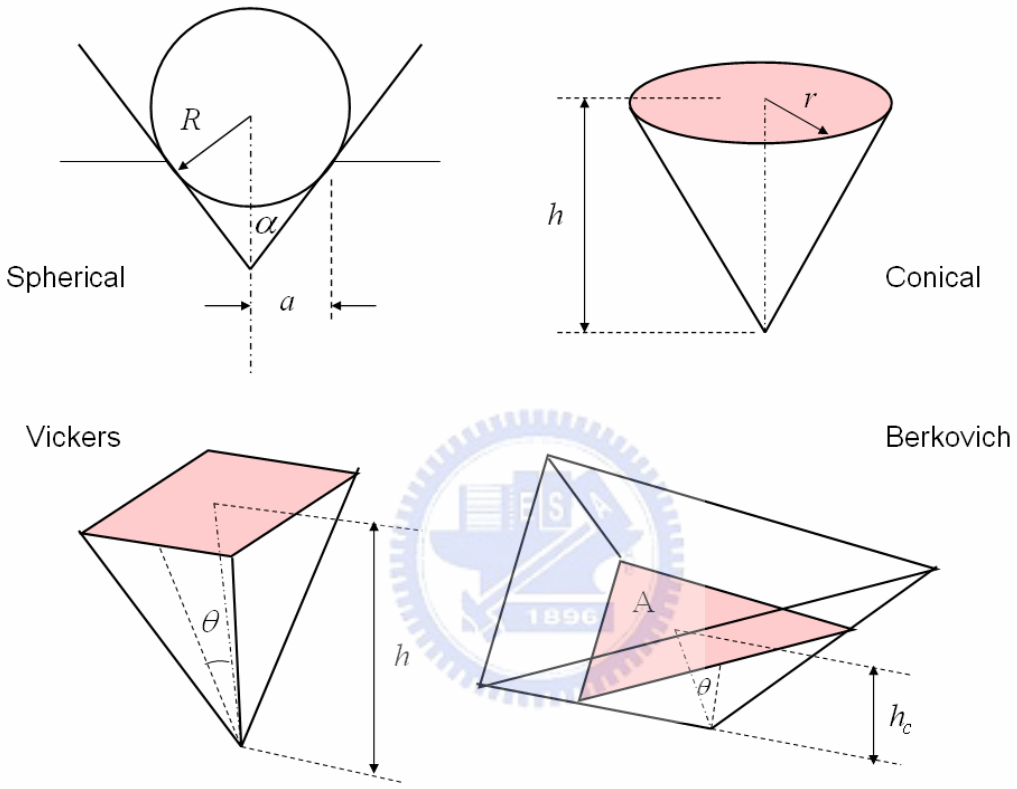

Figure A8. The geometry of indentation tips. Here, h_c is depth of penetration easured from the edge of the circle or area of contact. The related parameters can be seen in Table A1.

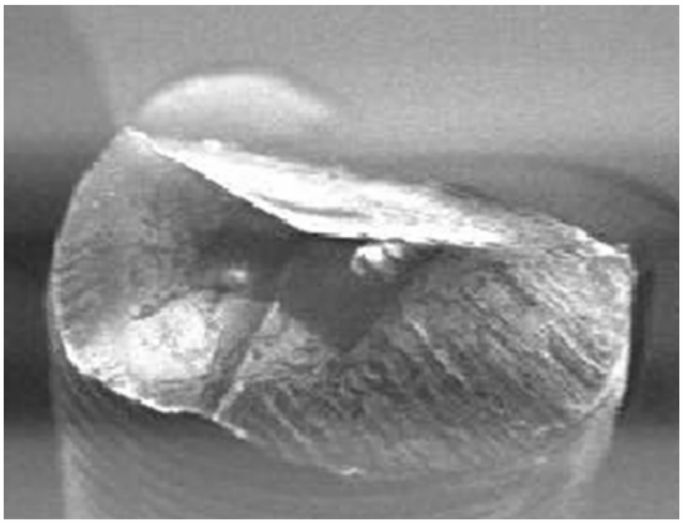

(a)

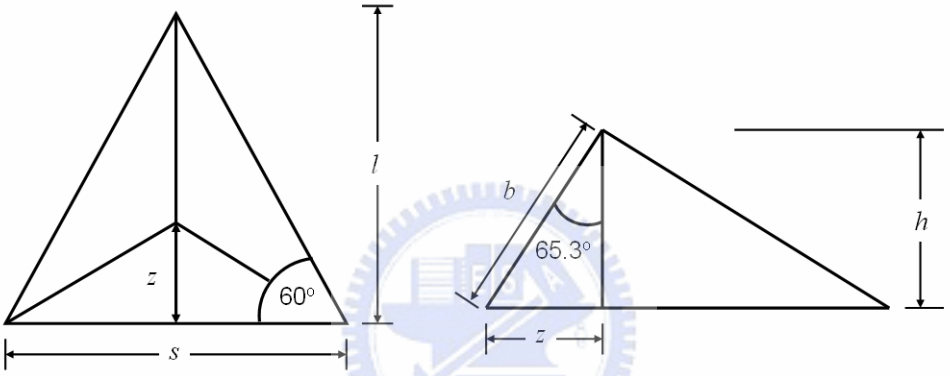

$$s = 2\sqrt{3}h\tan 65.3$$

$$z = \frac{s}{2}\tan 30$$

$$l = \frac{\sqrt{3}}{2}s$$

$$h = \frac{s}{2\sqrt{3}\tan 65.3}$$

$$b = \frac{s}{2\sqrt{3}\sin 65.3}$$

$$A_{pa} = 3\sqrt{3}h^2\tan^2 65.3 = 24.56h_c^2$$

Equivalent cone angle: 70.32°

(b)

Figure A9. (a) The image of a Berkovich indenter tip and (b) Schematic its equations for dimensions of tip indicate in schematics.

Appendix B

Molecular Dynamics Simulation Methodology

Basic understanding of the material properties often requires knowledge of the understanding energetic and interaction mechanism on a microscopic-level. In most situations this knowledge is not accessible to experimental tools. In these cases, which include the majority of material systems and phenomena, the use of computer-based techniques seems to promise particular success. They make it possible to obtain accurate numerical results about a complex system. Another merit of the computer simulation methods is that they can produce “macroscopic” behavior under precisely controlled conditions which can be varied by the observatory and, by so doing one can gain a great deal of physical insight into complex phenomena. Nowadays, the computer simulations are successfully applied to a wide range of problems in solid state physics, chemistry, material sciences and quantum field theory, opening so a new branch of investigations besides the experimental and theoretical methods.

While, in the early days, the computer simulations were limited to small systems with several hundred particles, large scale simulations are today possible and new

records in system sizes are reported frequently [1]. In this thesis, we make use of the *Molecular Dynamics* (MD) methodology, which is one of the computer-simulation techniques to recognize the nanoindentation-induced deformation mechanisms on semiconductors. A brief description of this method is given in the following sections.

MD was first used in thermodynamics and physical chemistry to calculate the collective or average thermochemical properties of various physical systems including gases, liquids and solids. It has been recently applied to simulate the instantaneous atomic behavior of a material system. There are two basic assumptions made in standard MD simulations:

1.) Molecules or atoms are described as a system of interacting material points, whose motion is described dynamically with a vector of instantaneous positions and velocities. The atomic interaction has a strong dependence on the spatial orientation and distances between separate atoms. This model is often referred to as the soft sphere model, in which the softness is analogous to the electron clouds of atoms.

2.) No mass changes in the system. Equivalently, the number of atoms in the system remains the same.

The simulated system is usually treated as an isolated domain with conserved energy.

B-1 MD simulation algorithms

In MD simulations for a system of $\mathcal{N}$ particulars, phase space exploration is achieved by numerical integration of the $3\mathcal{N}$ coupled Newton's motion equations:

$$m_i \frac{d^2 \vec{r}_i}{dt^2} = -\nabla_i \Phi\left(\vec{r}_1, \vec{r}_2, \ldots, \vec{r}_N\right), \tag{B1}$$

in discrete time steps Δt and a given set of thermodynamic variables (such as

volume, pressure and temperature). m_i denotes the mass of the ith particle, $\{\vec{r}_i\}$ the position vector of the particle and $\Phi(\{\vec{r}_i\})$ the potential energy of the system, oftenest written as the sum of interatomic pair potentials.

The time evolution of the system is determined, through a deterministic calculation of the trajectory of each particle in the phase space. This is in contrast to the Monte Carlo method [2], in which the system evolves according to stochastic dynamics by setting up a random walk to sample configuration via a given distribution function. To solve the Eq.(B1), we use a Gear's algorithm [3]. Gear's 5th predictor-corrector methods which require only one force evaluation per integration step Δt, as following:

∫ Predict

Particle positions $\vec{r}_i$ at time $t+\Delta t$ using a fifth-order Taylor series based on positions and their derivatives at time t. Hence, the derivatives $\dot{\vec{r}}_i$, $\ddot{\vec{r}}_i$, $\vec{r}_i^{(iii)}$, $\vec{r}_i^{(iv)}$ and $\vec{r}_i^{(v)}$ are needed at each time step; these are also predicted at time $t+\Delta t$ by applying Taylor expansions at t:

$$\vec{r}_i(t+\Delta t)=\vec{r}_i(t)+\dot{\vec{r}}_i(t)\Delta t+\ddot{\vec{r}}_i(t)\frac{(\Delta t)^2}{2!}+\vec{r}_i^{(iii)}(t)\frac{(\Delta t)^3}{3!}+\vec{r}_i^{(iv)}(t)\frac{(\Delta t)^4}{4!}+\vec{r}_i^{(v)}(t)\frac{(\Delta t)^5}{5!},$$

$$\dot{\vec{r}}_i(t+\Delta t)=\dot{\vec{r}}_i(t)+\ddot{\vec{r}}_i(t)\Delta t+\vec{r}_i^{(iii)}(t)\frac{(\Delta t)^2}{2!}+\vec{r}_i^{(iv)}(t)\frac{(\Delta t)^3}{3!}+\vec{r}_i^{(v)}(t)\frac{(\Delta t)^4}{4!},$$

$$\ddot{\vec{r}}_i(t+\Delta t)=\ddot{\vec{r}}_i(t)+\vec{r}_i^{(iii)}(t)\Delta t+\vec{r}_i^{(iv)}(t)\frac{(\Delta t)^2}{2!}+\vec{r}_i^{(v)}(t)\frac{(\Delta t)^3}{3!},$$

$$\vec{r}_i^{(iii)}(t+\Delta t)=\vec{r}_i^{(iii)}(t)+\vec{r}_i^{(iv)}(t)\Delta t+\vec{r}_i^{(v)}(t)\frac{(\Delta t)^2}{2!},$$

$$\vec{r}_i^{(iv)}(t+\Delta t)=\vec{r}_i^{(iv)}(t)+\vec{r}_i^{(v)}(t)\Delta t,$$

$$\vec{r}_i^{(v)}(t+\Delta t)=\vec{r}_i^{(v)}(t),$$

∫ Evaluate

From the above equations, the $\vec{r}_i(t+\Delta t)$ can be obtained. By using the Newton's motion equations to evaluate the force which acts on *i*th particle, i.e. $F_i(t+\Delta t)$.

∫ Correct

The predicted positions and their derivatives using the discrepancy $\Delta\ddot{\vec{r}}_i$ between *predict* and *evaluate* sections. And the equations of *predict* can be further corrected as follows:

$$\Delta\ddot{\vec{r}}_i = \left[\ddot{\vec{r}}_i(t+\Delta t) - \ddot{\vec{r}}_i^{\,P}(t+\Delta t)\right],$$

$$\vec{r}_i = \vec{r}_i^{\,P} + \alpha_0 \Delta R2\,,$$

$$\vec{r}_i \Delta t = \vec{r}_i^{\,P} \Delta t + \alpha_1 \Delta R2\,,$$

$$\frac{\ddot{\vec{r}}_i(\Delta t)^2}{2!} = \frac{\ddot{\vec{r}}_i^{\,P}(\Delta t)^2}{2!} + \alpha_2 \Delta R2\,,$$

$$\frac{\vec{r}_i^{(iii)}(\Delta t)^3}{3!} = \frac{\vec{r}_i^{(iii)P}(\Delta t)^3}{3!} + \alpha_3 \Delta R2\,,$$

$$\frac{\vec{r}_i^{(iv)}(\Delta t)^4}{4!} = \frac{\vec{r}_i^{(iv)P}(\Delta t)^4}{4!} + \alpha_4 \Delta R2\,,$$

$$\frac{\vec{r}_i^{(v)}(\Delta t)^5}{5!} = \frac{\ddot{\vec{r}}_i^{(v)P}(\Delta t)^5}{5!} + \alpha_5 \Delta R2\,, \qquad \text{where} \qquad \Delta R2 \equiv \frac{\Delta\ddot{\vec{r}}_i(\Delta t)^2}{2!},$$

The steps can be found to repeat that the procedures of *predict* section. In addition to that the values of α_i parameters in Gear's 5th Predictor-Corrector Algorithm are listed in Table B1.

B-2 Ensembles

In the traditional microcanonical MD simulations, one considers the movement of a constant number of particular in a box whose size and shape are fixed. The system is assumed to be free from any external force so that the total energy is conserved.

In this work, all the simulations are performed under constant volume $\mathcal{N}$ and temperature $\mathcal{T}$. This corresponds to the canonical ensemble ($\mathcal{N}$, $\mathcal{V}$, $\mathcal{T}$) in statistical mechanics. In this ensemble, the total energy is allowed to fluctuate by the interaction with a piston and through the thermal constant with a heat bath. The temperature $\mathcal{T}$ is related classically to the kinetic energy. We use this relation to realize the isothermal condition by scaling the velocities $\vec{v}_i$ of the particles

$$\vec{v}_i = \vec{v}_i \sqrt{3Nk_BT / \sum_{i=1}^{N} m_i \vec{v}_i^2} \ ,$$

in every time step Δt of the simulation. This simple velocity-scaling method, due to Woodcock [4], represents an approximation to the Gaussian constraint method [5], which realizes the correct canonical distribution in the coordinate space. The error of this approximation is of Δt, if the scaling is carried out at every time step.

B-3 Boundary conditions

Two limitations are imposed to MD simulations in the realization of the thermodynamic limit. On one side, there are finite-size effects in the simulations in the numerical system with a typical particles number $\mathcal{N}$ in the range of 10^3 is necessarily limited in size. A system of this size would be considerably affected by surface effects. On the other side, there is finite-observation-time effects in the simulation time is much shorter than the time used in experimental measurements. In

this work, we use the conventional *Periodic Boundary Conditions* (PBC) to minimize the finite-size effects. This approach consists in a periodic repetition of the simulation box in the three directions to fill the whole space. By construction, each particle possesses an infinity of periodic images. To avoid that a particle interacts with its own image or with two images of the same particle, the minimal-image convention is adopted [3]. Only interaction with the closest images is taken into account in this scheme. The range of the interaction is assumed to be smaller than $L/2$, where L is the length of the cubic box.

In order to minimize the finite-observation-time effects, the desired physical properties are evaluated by averaging the results over different configurations and over several MD runs using different starting configurations. The details can be found in Figs.B1-B2.

B-4 Cut-off radius methods

In modeling of materials, short-ranged potentials are usually used. The advantage of such potentials in MD simulations is evident: In a relatively large system, the number of particles pairs to be considered in the laborious forces calculations could be considerably reduced. In this present work, we describe the interatomic potentials mainly with Tersoff [6] many-body potentials which decay smoothly to zero at a distance r_c, the cut-off radius. For a given atom, the interactions are thus limited to the neighbors at distances smaller than r_c. The calculation of the different $N(N-1)/2$ distances in every integration step consumes a significant computing time. This can be considerably reduced by making use of the Verlet-list [3]. To every atom one attributes a neighbor list which contains all particles within a Verlet-radius r_V, chosen

somewhat larger than r_c. In calculating the forces acting on a given atom, only the particles belonging to its list are considered. The neighbor list is updated once every about 5 to 20 integration steps, depending on the mobility of the particles, such that the estimated maximal displacement of the particles between two updating remains smaller than the difference $r_V - r_c$. Please see the Fig.B3. Take note of the chosen σ value by using Verlet-list method. In general, the σ value is taken as 0.3 times the equipment distance of atoms.

Interatomic Potentials

The degree of correspondence between the MD simulation models and the physical system of interest depends to a large extent on the nature of the potential energy used in the simulations. The use of reliable potentials is therefore of a central importance for atomistic simulations.

In the simple models, the interaction between the atoms is described with pairwise interactions, the so-called pair potentials. These potentials have known deficiencies (e.g., a rigid but unrealistic correlation between cohesion and vacancy formation energy) which can be removed partly by going beyond the pair-potential picture and introducing some many-atom interactions. The pairwise potential and many-body potential can be simple described as illustrated in Fig.B4. We give in the following a brief description of some of these potentials.

B-5 Pair-potential interactions

There are two different approaches to describe the interatomic interactions in terms of pair potentials. The first approach is to write the total energy of an atomic arrangement as a sum over simple pair potentials

$$E_{total} = -\frac{1}{2}\sum_{i \neq j} \Phi_{ij}\left(\vec{R}_i - \vec{R}_j\right), \tag{B1}$$

where Φ and $\vec{R}$ denote as the pair potential and the atom coordinates, respectively. Rare gases and ionic systems, such as, can be adequately described in terms of these pair potentials. They include the Lennard-Jones potentials

$$\Phi(r) = 4\varepsilon\left[\left(\frac{\sigma}{r}\right)^{12} - \left(\frac{\sigma}{r}\right)^{6}\right], \tag{B2}$$

The first term is a short range positive contribution, modeling the electrostatic repulsion between the atoms. The second term is a negative contribution to the energy, representing the long range anisotropic van-der-Waals dispersion. The exponent 12 has been chosen for computational reason, the first term being the square of the second one. There are only two parameters, ε and σ, which correspond to the energy and time scale of the potential. The Lennard-Jones potential is well suited for rare gas, but yields only a crude description of other materials, due to its two-body function. A variety of other pair potentials have been suggested to describe materials other than rare gases. A widely used example is the Morse potential

$$\Phi(r) = \varepsilon\left(e^{-2\alpha(r-r_0)} - 2e^{-\alpha(r-r_0)}\right), \tag{B3}$$

which has three parameters to be fixed to the experimental properties of the materials.

The deficiency of simple pair potentials lies in their inability to reproduce many important properties of metals, e.g. the vacancy formation energy and the relation between the elastic constants.

The second approach to pair-potential description of the total energy is based on

their linear response theory and its mainly used in simple metals. In nearly-free-electron-like simple metals (non-transition metals) the valence electrons from a homogeneous electron gas and the ions can be described by weak pseudo-potentials. In the second order perturbation theory the total energy of the metal has the form [7]

$$E_{total} = -\frac{1}{2}\sum_{i \neq j} \Phi_{ij}\left(\vec{R}_i - \vec{R}_j\right) + E_{vol}\,, \tag{B4}$$

where E_{vol} is an energy term independent of the structure of the metal but dependent on the total volume of the system. In this approach, the pair pseudo-potential Φ has a very different meaning than the expression of Eq.(B1) since only part of the total energy comes from the sum over the pair potentials (in Al, for example, the pair-potential sum gives only a few percent of the cohesion energy). Generally, the interatomic potentials based on the pseudo-potential approach work fairly well for those properties of the metals where the density fluctuations are small. In the case of surfaces and open volume defects, such as vacancies, these potentials are, however, inappropriate since the density changes are so large that they cannot be described by the linear response theory.

B-6 Many-atom interactions

For metallic system, an alternative to the pair potential picture is provided by the *Effective Medium Theory* (EMT) [8] or the related *Embedded Atom Method* (EAM) [9]. This approach is based on the ideas of the *Density-Functional Theory* (DFT) [10] (and amenable to MD-simulation modeling). Here the total energy of the metal can be written as

$$E_{total} = \sum_i F(n_i) + \frac{1}{2}\sum_{i \neq j} \Phi_{ij}\left(\vec{R}_i - \vec{R}_j\right), \tag{B5}$$

where n_i is an effective electron density at the site of the atom i and its approximated by the superposition of atomic density tails from the order atoms

$$n_i = \sum_i n_{at,i}\left(\left|\vec{R}_i - \vec{R}_j\right|\right), \tag{B6}$$

$F(n_i)$ is a nonlinear function (the "embedding energy") describing the interaction of the atom i with its electronic surrounding and Φ is a pair potential. The embedding-energy term $F(n_i)$ is supposed to describe the complex many-atom interactions. Moreover, it is an explicit function of atomic positions so that variations in local atom density can be easily accounted for. F, n_i and Φ can be derived theoretically or determined empirically by choosing proper parameterization functions and fitting the parameters to some experimental data.

Compared to pair potentials, EAM derived potentials include higher-body interactions. The empirical method, in term of Eq.B5, was the EAM model introduced by Daw and Baskes [9]. In Ref.9, the pair potential Φ is a purely repulsive term accounting for ion-ion and orthogonalization repulsion at short range. Since this work, several other methods, equivalent to the EAM, have been proposed. These methods all take the form of Eq.(B5) with differences due to specific parameterizations of F and n_i. Finnis and Sinclair [11] proposed that the d-d hybridization in the second-moment approximation of the tight-binding model could also be described by Eq.(B5). The energy function F is found then to be negative and can be thought to be proportional to the negative square root of the coordination number. The advantage of the total energy expression of Eq.(B5) is that it is essentially as efficient in computer simulations as the pair-potential expressions of Eq.(B1) or Eq.(B4). Furthermore, EAM potentials have been found to describe fairly well bulk and surface properties of transition metals. Similar good results have been obtained using the tight-binding

model of Finnis and Sinclair [11]. Moriarty [12] has extended the pseudo-potential theory to higher order of perturbation to derive three-body forces and higher many-body interactions to the elemental transition metals. However, as this approach is based on a uniform electron gas as starting point, it is not expected to be adequate, even in higher orders, for studying inhomogeneous defect environments; e.g. the structure of surfaces where the electron density goes to zero.

EAM class of potential is well adapted for metals, because of the bond order term that mimics the hardness of metallic bonds as a function of the function of the coordinate. This approach has proved to be inadequate for semiconductors, in which covalent bonds have a complicated dependence on coordination and bond angles. This is actually the case for semiconductors of Group IV, such as diamond, Si, Ge or SiC, stable in a diamond cubic or zincblende structure. Due to their technological importance, several kinds of potentials have been designed for these materials. For example, an extended version of the EAM model has been developed [13], with angle-dependent electron densities. Another one, the Stillinger-Weber potential, for which sets of parameters for Si and Ge are available, has been widely used [14]. Its function is written below:

$$E = \sum_{i,j} \varepsilon F_2\left(\frac{\left|\vec{R}_i - \vec{R}_j\right|}{\sigma}\right) + \sum_{i,j,k} \varepsilon F_3\left(\frac{\vec{R}_i}{\sigma}, \frac{\vec{R}_j}{\sigma}, \frac{\vec{R}_k}{\sigma}\right), \tag{B7}$$

$$F_3\left(\vec{R}_i, \vec{R}_j, \vec{R}_k\right) = h\left(R_{ij}, R_{ik}, \theta_{jik}\right) + h\left(R_{ji}, R_{jk}, \theta_{ijk}\right) + h\left(R_{ki}, R_{kj}, \theta_{ikj}\right), \tag{B8}$$

F_2 and h are two analytical functions, vanishing beyond a given cutoff. F_3 is a three-body contribution introducing an angular dependence in the energy. The energy gain is maximal for the bond angle of the diamond cubic structure. Compared to pair potentials, an additional term of the Born-Oppenheomer development is included in the potential function, what improves the accuracy of interatomic forces description.

In addition, this term bears an angular dependence, particular well suited for covalent materials where bonds are directional.

The dependence of the interactions on the local environment is strengthened by taking into account three-body terms. However, this approach requires a larger computational effort, since during the calculation interactions have to be computed for all atomic triplets. It is possible to use a two-body function while introducing environment dependence by modifying the interactions as a function of the atomic environment of the atoms. An example is given by the potential of Tersoff [15], which is available for diamond, Si, Ge and compounds such as SiC and SiGe alloys [6].

$$E = \frac{1}{2}\sum_{i \neq j} f_C\left(\left|\vec{R}_i - \vec{R}_j\right|\right)\left[f_R\left(\left|\vec{R}_i - \vec{R}_j\right|\right) + b_{ij}\, f_A\left(\left|\vec{R}_i - \vec{R}_j\right|\right)\right], \tag{B9}$$

Here, f_R and f_A are repulsive and attractive functions, respectively, while f_C is a function going smoothly to zero beyond a given cut-off. The bond order contributions are included through b_{ij}, which is modified according to local environment as a function of interatomic distances and angles. The Tersoff potential is different from the EAM approach in the sense that the two-body Tersoff interactions are directly modified by local environment, while bond order is obtained in EAM via electron distributions.

B-7 Model used in this work

We describe in this appendix the interatomic potentials employed in this work to study the indentation model. Tersoff's potential has been the most successful that it reproduces many of the properties of the semiconductors. Here, MD simulation is carried out for the indentation model (C/GaAs) by means of Tersoff's potential [6]. The form of the energy E, between two neighboring

atoms *i* and *j*, as follows:

$$E = \sum_i E_i = \frac{1}{2}\sum_{i \neq j} u_{ij} \ , \tag{B10}$$

with

$$u_{ij} = f_C(r_{ij})\left[f_R(r_{ij}) + b_{ij}\, f_A(r_{ij})\right] \ , \tag{B11}$$

where

$$f_R(r_{ij}) = A_{ij} \exp(-\lambda_{ij} r_{ij}) \quad , \quad f_A(r_{ij}) = -B_{ij} \exp(-\mu_{ij} r_{ij}), \tag{B12}$$

$$f_C(r_{ij}) = \begin{cases} 1 & r_{ij} < R_{ij} \\ \frac{1}{2} + \frac{1}{2}\cos\left[\frac{\pi(r_{ij} - R_{ij})}{S_{ij} - R_{ij}}\right] & R_{ij} < r_{ij} < S_{ij} \\ 0 & r_{ij} > R_{ij} \end{cases}, \tag{B13}$$

b_{ij} is the many-body order parameter describing how the bond-formation energy is affected by the local atomic arrangement owing to the presence of other neighboring atoms (the *k* atom). It is a many-body function of the positions of atoms *i*, *j* and *k*. It has the form

$$b_{ij} = \chi_{ij}\left(1 + \beta_i^{n_i} \zeta_{ij}^{n_i}\right)^{-1/2n_i}, \tag{B14}$$

with

$$\zeta_{ij} = \sum_{k \neq i,j} f_C(r_{ik})\, g(\theta_{ijk}) \quad , \quad S_{ij} = \sqrt{S_i S_j} \quad , \tag{B15}$$

$$g(\theta_{ijk}) = 1 + \frac{c_i^2}{d_i^2} - \frac{c_i^2}{d_i^2 + (h_i - \cos\theta_{ijk})^2} \quad , \tag{B16}$$

$$\begin{aligned} \lambda_{ij} &= \frac{1}{2}(\lambda_i + \lambda_j) \quad , \quad \mu_{ij} = \frac{1}{2}(\mu_i + \mu_j) \\ A_{ij} &= \sqrt{A_i A_j} \qquad , \quad B_{ij} = \sqrt{B_i B_j} \end{aligned}, \tag{B17}$$

Here, ζ is called the effective coordination number and $g(\theta)$ is a function of the angle between r_{ij} and r_{ik} that has been fitted to stabilize the structure. The parameters between two different materials are calculated by using the mixing rules. The other parameters can be found in [6, 16-17] and listed in Table B2.

B-8 MD calculation Flowchart

The simulated flowchart is displayed in Fig.B5, as following:

(1). The total atoms of system, the radius of an atom, the distance of cut-off radius, the interval of integrating time, the end computing conditions and the boundary conditions were set up, and then the system was computed by the simulated potential model.

(2). The interaction forces between two atoms were computed from the potential model of system.

(3). By using the combined Verlet-list and Cell-link methods to find the interacted atoms with *i*th atom, further to establish the list table.

(4). To obtain the initial position and velocity by integrating the Newton's motion equations.

(5). Taking the input data and the simulated conditions into the continuous equations to obtain the position and velocity of atoms on next steps.

(6). And then the position and velocity of atoms at different times were computed.

(7). According to the boundary conditions, the position of atoms was computed and modified further.

(8). The procedures (5)–(7) were repeated until the computed processes were performed for all atoms.

(9). Then the total interaction forces and positions of atoms in every step were output.

(10). Finished.

References

1. J. Stadler, R. Mikulla and H.R. Trebin, Int. J. Mod. Phys. C 8 (1997) 1131.
2. M.P. Allen, D.J. Tildesly, *Computer Simulation of Liquids* (Clarendon Press, Oxford 1987).
3. J.M. Haile, *Molecular Dynamics Simulation: Elementary Methods* (Wiley, New York, 1992).
4. L.V. Woodcock, Chem. Phys. Lett. 10 (1971) 257.
5. S. Nosé, Progr. Theoretical Physics Suppl. 103 (1991) 1.
6. J. Tersoff, Phys. Rev. B 39 (1989) 5566.
7. W.A. Harrison, *Pseudopotential in the Theory of Metals* (Benjamin, New York 1966).
8. J.K. Nørskov and N.D. Lang, Phys. Rev. B 21 (1980) 2131.
9. M.S. Daw and M.I. Baskes, Phys. Rev. Lett. 50 (1983) 1285.
10. H. Hohenberg and W. Kohn, Phys. Rev. B 136 (1964) 864.
11. M.W. Finnis and J.R. Sinclair, Phil. Mag. A 50 (1986) 45.
12. J.A. Moriarty and M. Widom, Phys. Rev. B 56 (1997) 7905.
13. M.I. Baskes, Phys. Rev. B 46 (1992) 2727.
14. F.H. Stillinger and T.A. Weber, Phys. Rev. B 31 (1985) 5262.
15. J. Tersoff, Phys. Rev. B 38 (1988) 9902.
16. M. Nakamura, H. Fujioka, K. Ono, M. Takeuchi, T. Mitsui and M. Oshima, J. Crystal Growth 209 (2000) 232.
17. W.H. Moon and H.J. Hwang, Phys. Lett. A 315 (2003) 319.

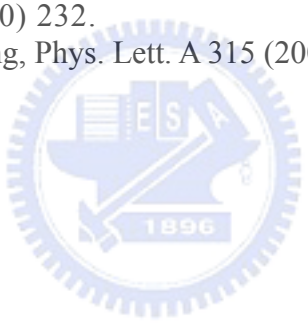

Table and Figure Captions

Table B1. Values of α_i parameters in Gear's 5th Predictor-Corrector Algorithm for second-order differential equations using predictors of order q.

α_i	$q=3$	$q=4$	$q=5$
α_0	$\frac{1}{6}$	$\frac{19}{120}$	$\frac{3}{16}$
α_1	$\frac{5}{6}$	$\frac{3}{4}$	$\frac{251}{360}$
α_2	1	1	1
α_3	$\frac{1}{3}$	$\frac{1}{2}$	$\frac{11}{18}$
α_4	—	$\frac{1}{12}$	$\frac{1}{6}$
α_5	—	—	$\frac{1}{60}$

Table B2. Parameters used for the MD simulation of C, Ga and As.

	C	$Ga-Ga$	$As-As$	$Ga-As$
$A(eV)$	1393.6	2839.821	4773.163	13287.605
$B(eV)$	346.7	114.786	81.32	13.187
λ	34.879	3.2834	3.4841	4.5989
μ	22.119	1.7154	1.7154	0.2493
$R(nm)$	0.18	3.4	3.4	3.4
$S(nm)$	0.21	3.6	3.6	3.6
β	1.5724×10^{-7}	0.2358624	0.0074881	0.357192
n	0.72751	3.4729041	0.6087913	6.31747
c	3.8049×10^{4}	0.0762977	5.2731318	1.226302
d	4.384	19.796474	0.7510266	0.790396
h	-0.57058	7.1459174	0.1529235	-0.518489

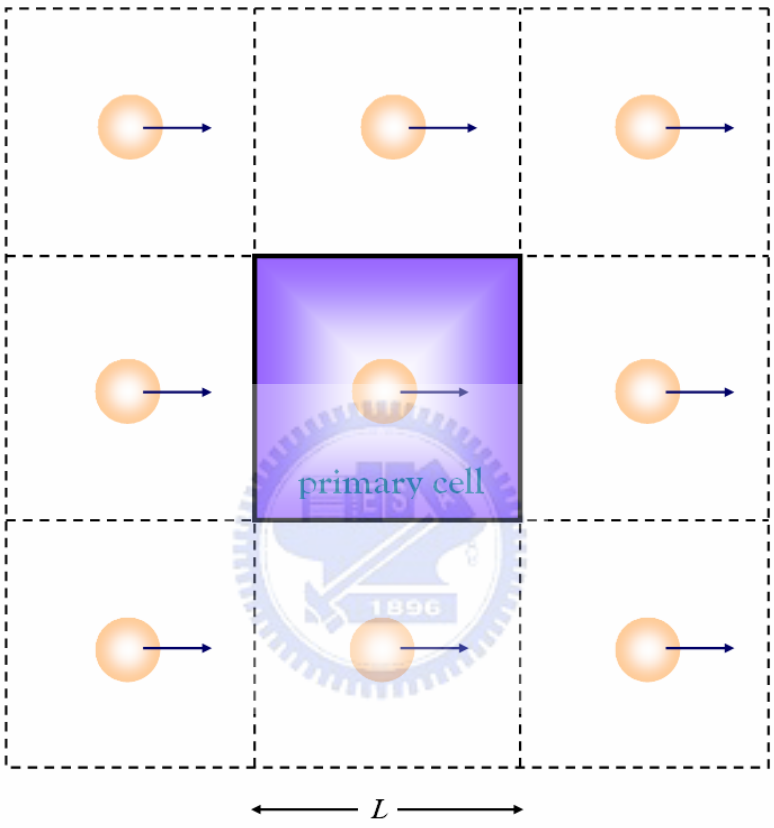

Figure B1. Schematic of periodic boundary condition.

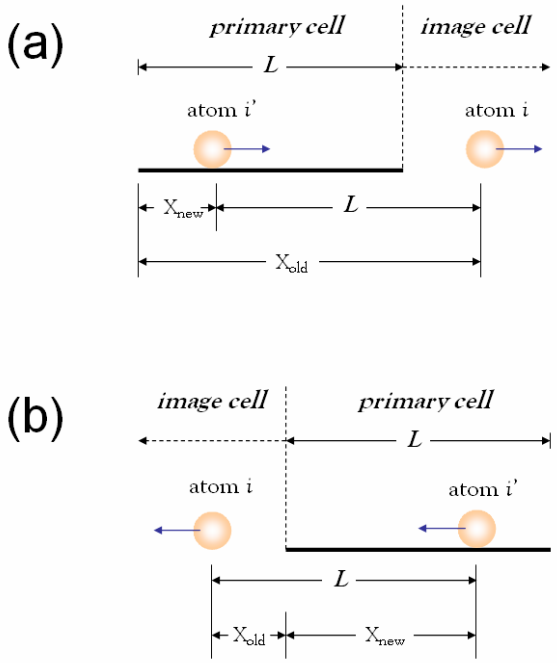

Figure B2. Using the behavior of atoms move along the x-direction to explain the PBC conditions within the primary cell: (a) if X_{old} > L, set $X_{new} = X_{old} - L$, where X_{old} is an initial position of the atom, L is the length of the primary cell and X_{new} is the new modified position; (b) if Xold < 0, set $X_{new} = X_{old} + L$. Then considering the minimum image criterion: (c) the distance between the atom i and atom i+1 is X_{old}, the modified distance between the atom i and atom i+1 is X_{new}. When $X_{old} > L/2$, the distance between the atom i' and atom i+1 is X_{new} which has taken the place of X_{old}; (d) when $X_{old} < -L/2$, the distance between the atom i' and atom i+1 is X_{new} which has taken the place of X_{old}.

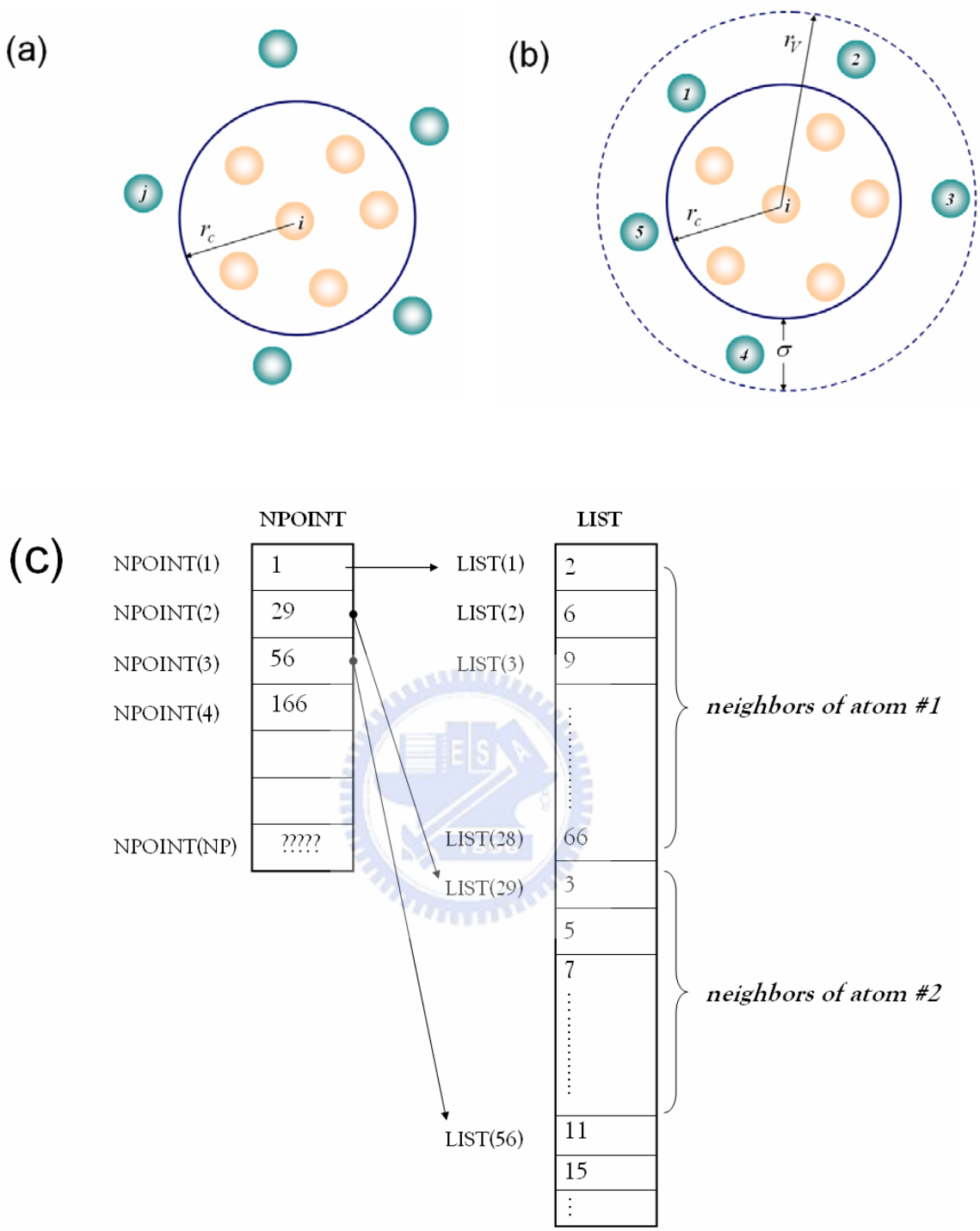

Figure B3. (a) Schematic of cut-off radius; (b) and (c) show the Verlet-list method. Use of two one-dimensional arrays to store a neighbor list for each atom during a simulation of a system containing N atoms. NPOINT(NP) and LIST are the memory positions in the computer.

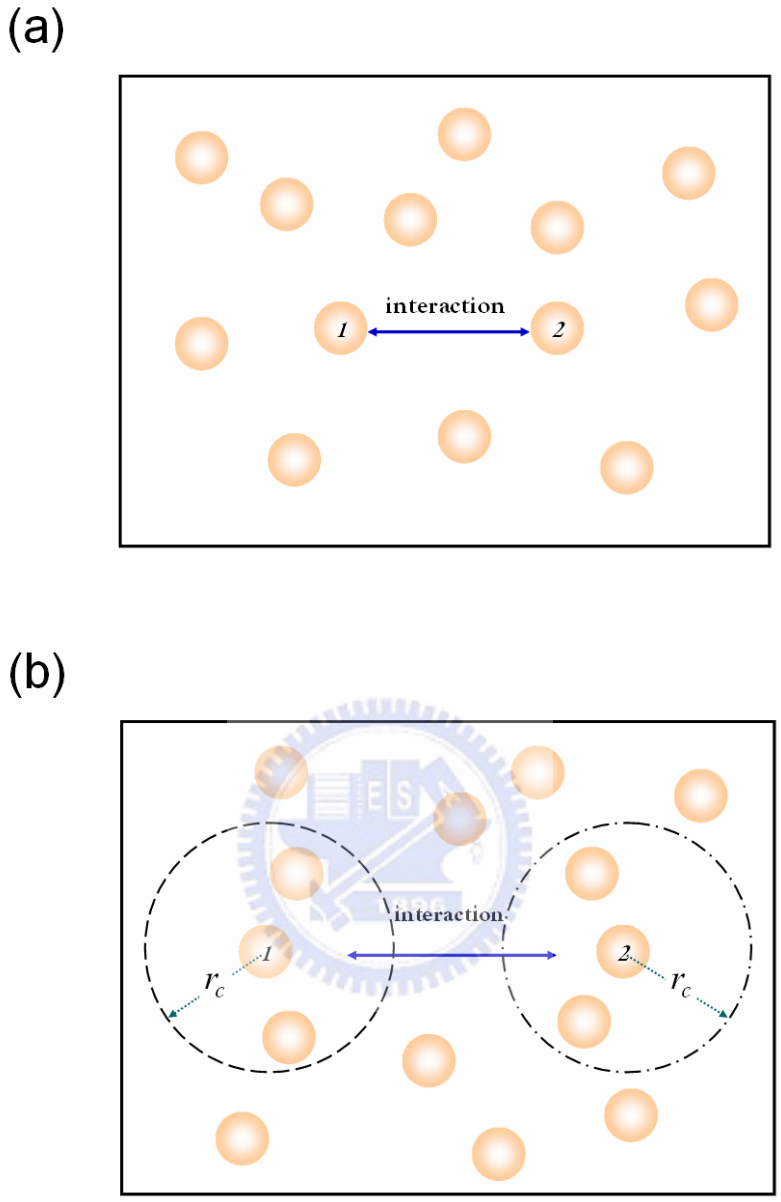

Figure B4. (a) Pairwise potential: the interaction of atom 1 and atom 2 within the cut-off radius is considered only; (b) Many-body potential: besides the interaction of atom 1 and atom 2, the interactions of others atoms within the cut-off radius are also considered.

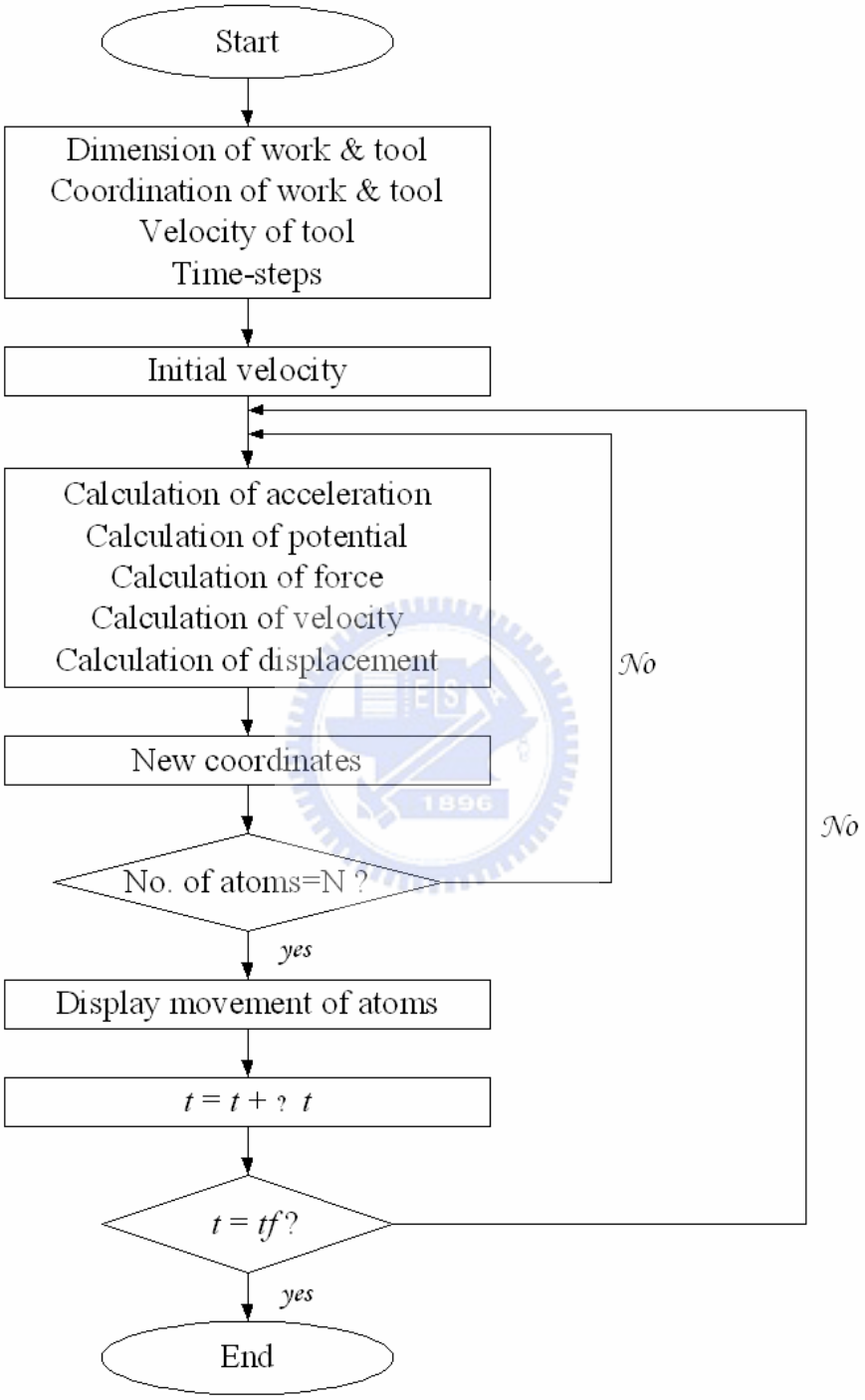

Figure B5. The flowchart of Molecular Dynamics Simulations.

Appendix C

Dislocations

A dislocation is a one-dimensional line defect which causes lattice distortion around that line. Dislocations are permanent or plastic deformations. They exert a profound effect on structure sensitive properties such as hardness, strength, toughness and ductility. They may move under influence of external forces which produce stress in the crystal. The area swept by the movement is called the glide plane. Dislocations by definition are always on the glide plane. There are two dislocations types:

1). Screw dislocation: A screw dislocation occurs as atoms go around in a rotation and form a spiral ramp. The Burgers vector of an edge dislocation is normal to the line of the dislocation.

2). Edge dislocation: An edge dislocation is created as an extra half plane of atoms is inserted. The Burgers vector of a screw dislocation is parallel to the line of the dislocation.

C-1 Dislocations in Crystals

∫ Burgers vector

The Burgers vector determines the direction of a dislocation and its magnitude. To produce the vector, a circuit is created by jumping from atom to atom. On a perfect lattice, with the same number of jumps to each direction, the starting point of the circuit and the ending point are the same. This is not necessarily the case when there is a dislocation, in which there may be a closing failure. The failure is defined to be the Burgers vector. In an edge dislocation, the Burgers vector is on the same plane of the circuit and perpendicular to the dislocation line. In contrary, in a screw dislocation, it is parallel to the dislocation line. The Burgers vector of a perfect dislocation is composed from the original lattice vectors. Imperfect dislocations occur as the Burgers vector is not a composition of original lattice vectors.

The general equations for a screw dislocation, depending on the Burgers vector, as following [1]:

$$u_x = 0,$$
$$u_y = 0,$$
$$u_z = \frac{b}{2\pi}\arctan\frac{y}{x}$$

when the dislocation line is on the *z*-axis. *u* is the displacement vector of an atom, with u_x, u_y and u_z its components to each axis. Note of the atoms are dislocated normal to the dislocation line, on the *x*- and *y*-direction. The dislocations are only in parallel to the dislocation line. On the other hand, the general equations foe an edge dislocation that is slightly more complicated, as following [1]:

$$u_x = \frac{b}{2\pi}\left[\arctan\frac{y}{x} + \frac{xy}{2(1-v)(x^2+y^2)}\right],$$

$$u_y = -\frac{b}{2\pi}\left[\frac{1-2v}{4(1-v)}\ln(x^2+y^2) + \frac{x^2-y^2}{4(1-v)(x^2+y^2)}\right],$$

$$u_z = 0$$

The atoms are dislocated on the *x*-*y* plane which is normal to the dislocation line. Note that there is no dislocation on the *z*-direction, parallel to the dislocation line.

∫ Miller indices

A plane with Miller indices ($m_1m_2m_3$) is parallel to a plane cutting the axes at $1/m_1$, $1/m_2$, $1/m_3$ where m_i are integers. The direction notation [$n_1n_2n_3$] represents the vector $n_1\vec{a}_1 + n_2\vec{a}_2 + n_3\vec{a}_3$, where n_i are integers and, a_1, a_2, a_3 are primitive vectors which define the crystal axes. The notation {$m_1m_2m_3$} represents the set of equivalent planes of the type ($m_1m_2m_3$) which are equivalent by symmetry and similarly ⟨$n_1n_2n_3$⟩ represents the set of all directions of the type [$n_1n_2n_3$].

∫ Core structure

Close-packed structures have layers of atoms in the position A, B and C as illustrated in Fig.C1. The sequence of stacking the layers defines the structure type of the crystal. A FCC-type structure has a stacking sequence of ABCABCABC…, while a Hexagonal Close Packed (HCP) has a stacking sequence of ABABAB…. Close-packed structures, such as the FCC, can have dislocations which are called stacking faults (SFs). They are faults by mismatching close-packed planes as the crystal deforms or grows. SFs are significantly in the deformation of metals in closed-packed structures because they affect the ease of a dislocation slipping from one to another. An example of a SF occurring in a FCC is ABCABCBCABC, missing

the layer A (intrinsic SF, ISF). Another is ABCABCBABCABC, with extra layer B inserted (extrinsic SF, ESF). These dislocations have Burger vectors which are not a translation vector of the FCC lattice. They are known as Frank partial dislocations.

A partial dislocation loop can be viewed as the boundary separating an area of ISF from the rest of the plane. This partial shift can occur in any of the three equivalent directions $\vec{b}_{p1}, \vec{b}_{p2}, \vec{b}_{p3}$, as illustrated by the arrows in Fig.C1(b). To make a complete (perfect) dislocation, two atomic layers bounding the ISF inside the first partial loop have to be shifted again along another partial shift direction. Clearly, for every perfect dislocation with Burgers vector $\vec{b}$, only one combination of partial shift $\vec{b}_{p1}$ and $\vec{b}_{p2}$ exists that avoids atomic run-ons and then only if introduced in a certain order. This simple observation lies behind the well-known leading-trailing partial rule usually formulated using the Thompson tetrahedron notation, please see Fig.C2. Much of the dislocation behavior observed in FCC materials results from the Shockley dissociation, by which perfect $\frac{1}{2}<110>$ dislocations split into two partial dislocations, bounding an area of SF. Expressed in Miller index notation such a reaction reads

$$\frac{1}{2}[110] = \frac{1}{6}[21\bar{1}] + SF + \frac{1}{6}[121]$$

While the reduction of elastic energy achieved by this dissociation is considerable, this reaction can occur only if a stable low-energy SF exists. In FCC materials stable SFs are found only in the {111} planes. The dissociated dislocations glide in the planes containing the SFs which simply move along with the partial dislocations. We emphasize that it is the availability of stable SFs in the {111} planes that defines the well-known predisposition for dislocation to glide on these planes.

C-2 Deformation twinning

A twin refers to a region within a lattice that can be described as either a reflection across the boundary between the parent lattice and the twin or a rotation of 180° about a specific axis. Often both the reflection and rotation descriptions are simultaneously accurate and, in either case the bulk structure of the twinned region is equivalent to that of the original lattice. The twin boundary is therefore critical in describing the energetics if this defect. The shaded region in Fig.C3 is a schematic of a twinned structure, which exhibits a reversal of stacking order that can be described by a mirror plane at the twin boundary.

Both dislocation slip and deformation twinning are shown in Fig.C4. These are the two primary deformation mechanisms exhibited by a crystal lattice to accommodate large strains. In Fig.C4, each sheet represents a crystallographic plane of atoms. The picture of an undeformed lattice is shown in Fig.C4(a). The elastic regime for shear deformation can be described by homogeneous shear strain in which each plane is displayed relative to the plane below it by some common distance, as illustrated in Fig.C4(b). Dislocation slip is displayed in Fig.C4(c) where a single pair of planes is displaced relative to one another by a full lattice spacing in the shear direction and thereby accommodates strain for the entire crystal lattice. Deformation twinning where many adjacent pairs of planes are displaced relative to one another, please see Fig.C4(d). This creates the reorientation of the original lattice that can be described by the reflection across a twin boundary as illustrated in Fig.C3.

According the above mentioned, a schematic of a {111} plane in the FCC structure in which a full Burger's vector, b, is found along the ⟨110⟩ directions. The full Burger's vector can be dissociated in to partial Burger's vectors, b_p, in the ⟨112⟩ directions. In addition the three positions labeled A, B and C indicate the stacking

sequence for the {111} close-packed planes in the FCC structure. The favorable twinning system for the FCC materials that are the $\{111\}<11\bar{2}>$ with each atom being displaced in a full formed twin by the partial Burger's vector $\frac{1}{6}[11\bar{2}]$ on the {111} plane. This displacement corresponds to an ISF in the FCC lattice. Nevertheless, when a succession of adjacent planes are displaced relative to each other by a partial Burger's vector they form a FCC lattice with a reversed stacking sequence from the parent lattice, which is a twinned structure.

References

1. J.P. Hirth and J. Lothe, Theory of dislocations, (McGraw-Hill, New York, 1968.)

Figure Captions

Figure C1. (a) Plane-on view of {111} plane of FCC lattice; (b) Perfect Burgers vectors $\vec{b}_{1,2,3}$ *and partial Burgers vectors* $\vec{b}_{p1,p2,p3}$ *on {111} plane.*

Figure C2. Thompson tetrahedron notation for FCC slip systems.

Figure C3. Schematic of a twinned lattice described by reflection across a mirror plane, which can be seen by the reversal of the stacking sequence across the twin boundary.

Figure C4. Illustration of lattice deformation mechanisms. The undeformed lattice is given for reference in (a) compared to elastic deformation via homogeneous shear stress (b) and, two plastic deformation mechanisms, dislocation slip (c) and, deformation twinning (d).

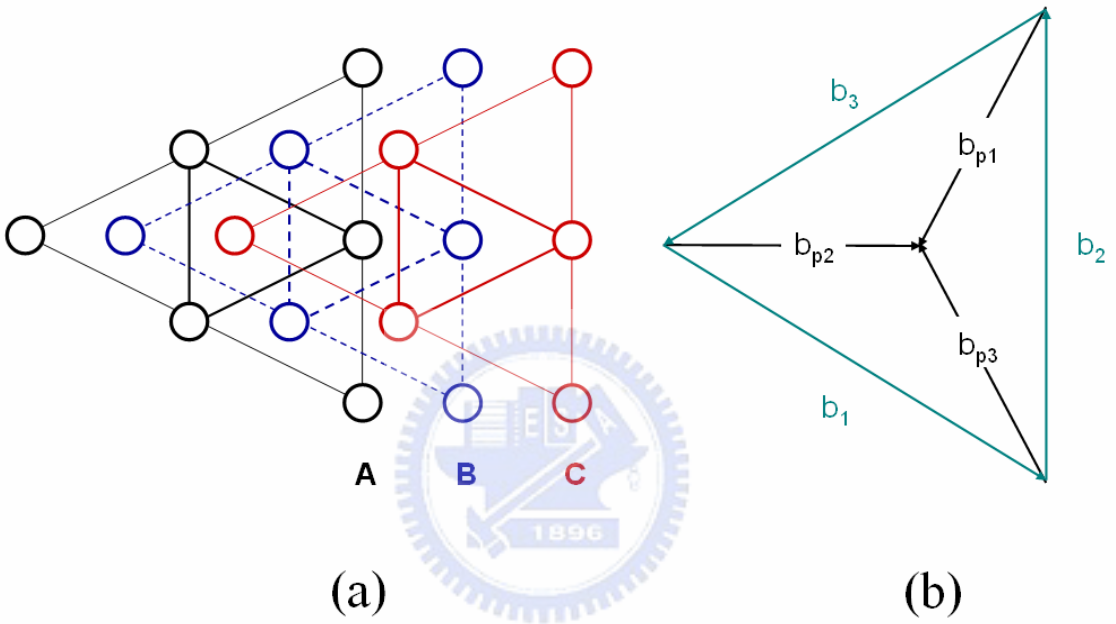

Figure C1. (a) Plane-on view of {111} plane of FCC lattice; (b) Perfect Burgers vectors $\vec{b}_{1,2,3}$ *and partial Burgers vectors* $\vec{b}_{p1,p2,p3}$ *on {111} plane.*

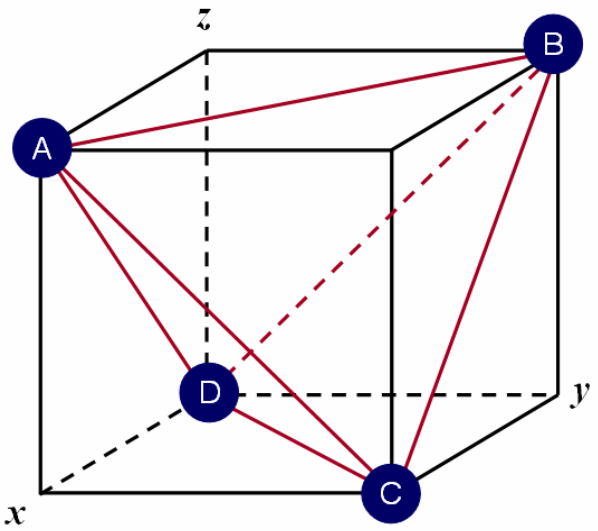

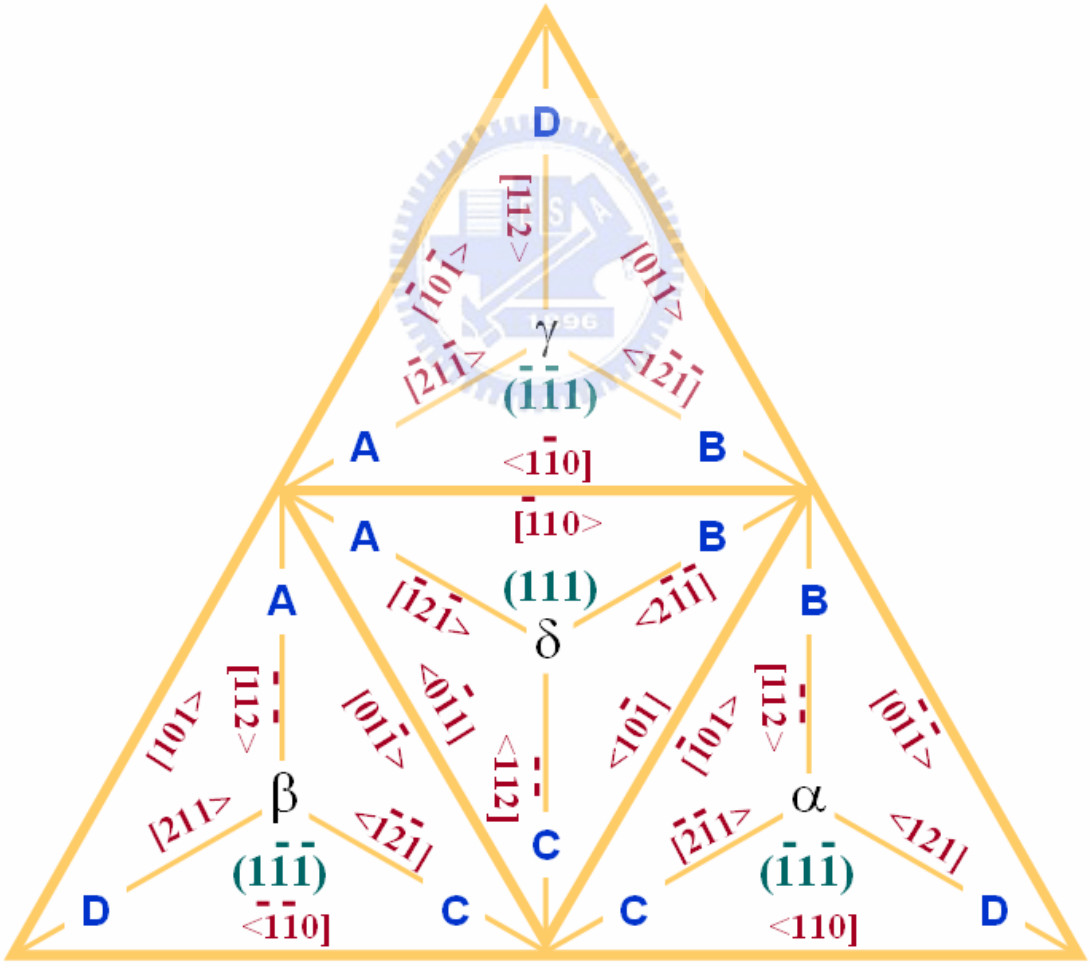

Figure C2. Thompson tetrahedron notation for FCC slip systems.

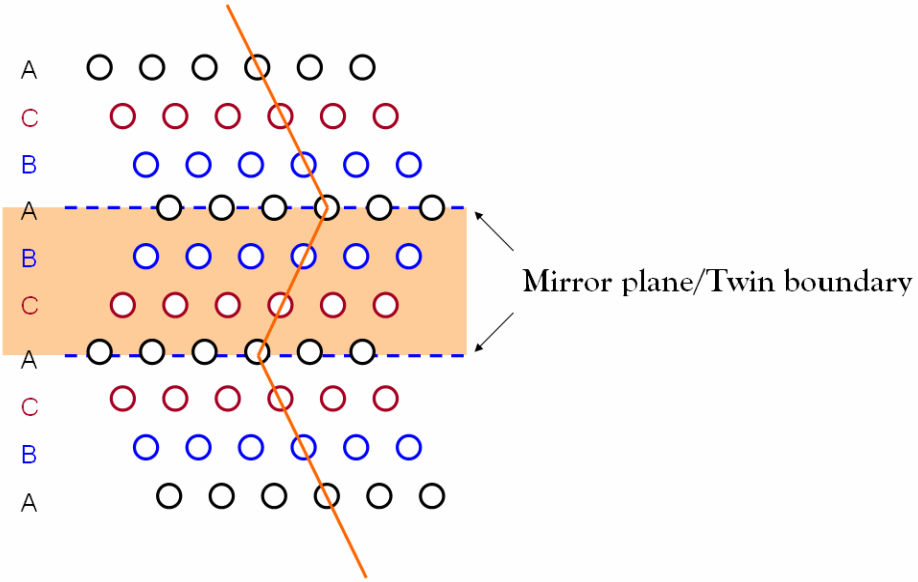

Figure C3. Schematic of a twinned lattice described by reflection across a mirror plane, which can be seen by the reversal of the stacking sequence across the twin boundary.

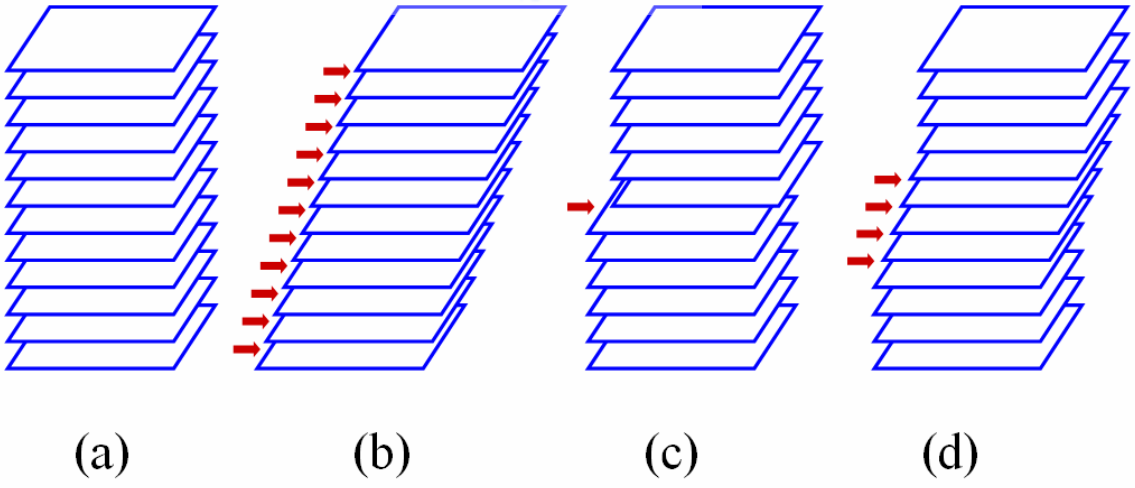

Figure C4. Illustration of lattice deformation mechanisms. The undeformed lattice is given for reference in (a) compared to elastic deformation via homogeneous shear stress (b) and, two plastic deformation mechanisms, dislocation slip (c) and, deformation twinning (d).